A study of the shortwave direct aerosol forcing using ESSP/CALIPSO observation and GCM simulation

Oikawa, Eiji
Atmosphere and Ocean Research Institute, University of Tokyo

Nakajima, Teruyuki
Atmosphere and Ocean Research Institute, University of Tokyo

Inoue, Toshiro
Atmosphere and Ocean Research Institute, University of Tokyo

Winker, David
NASA Langley Research Center

出版情報：Journal of Geophysical Research: Atmospheres. 118 (9), pp.3687-3708, 2013-05-16. American Geophysical Union
バージョン：

A study of the shortwave direct aerosol forcing using ESSP/CALIPSO observation and GCM simulation

Eiji Oikawa,[1] Teruyuki Nakajima,[1] Toshiro Inoue,[1] and David Winker[2]

Received 6 January 2012; revised 4 September 2012; accepted 25 January 2013; published 13 May 2013.

[1] Shortwave direct aerosol radiative forcing (DARF) is derived at the top of the atmosphere (TOA) and at the surface under clear-sky, cloudy-sky, and all-sky conditions using data of space-borne CALIOP lidar and MODIS sensor. We investigate four scenarios for evaluating the DARF: clear-sky, the case that aerosols exist above clouds, the case that aerosols exist below high-level clouds, and the case that aerosols are not detected by CALIOP in cloudy-sky condition. The cloudy-sky DARF is estimated by the latter three scenarios. The all-sky DARF is the combination of clear-sky and cloudy-sky DARF weighted by the cloud occurrence. They are then compared with DARF calculated by a global aerosol model, SPRINTARS. The results show that the TOA forcing over desert regions caused by dust with single scattering albedo (SSA) of 0.92 is positive regardless of cloud existence, due to high solar surface albedo. Off southern Africa, smoke aerosols with SSA of 0.84 above low-level clouds are observed and simulated and the annual mean TOA cloudy-sky DARF is estimated at more than +3 Wm^{-2}, consistent with past studies. Aerosols with SSA of 0.96 within optically thin clouds cause a TOA negative forcing, while that within optically thick clouds cause a TOA positive forcing. This indicates that aerosols within optically thick clouds cause positive forcing in our radiative transfer calculation, regardless of SSA. Annual zonal averages of DARF from 60°S to 60°N under clear-sky, cloudy-sky, and all-sky are −2.97, +0.07, and −0.61 Wm^{-2} from CALIOP and −2.78, +1.07, and −0.58 Wm^{-2} from SPRINTARS.

Citation: Oikawa, E., T. Nakajima, T. Inoue, and D. Winker (2013), A study of the shortwave direct aerosol forcing using ESSP/CALIPSO observation and GCM simulation, *J. Geophys. Res. Atmos.*, *118*, 3687–3708, doi:10.1002/jgrd.50227.

1. Introduction

[2] Anthropogenic and natural aerosols affect the Earth's radiation budget both directly and indirectly. The aerosol direct effect occurs by direct scattering and absorption of solar and thermal radiation. The aerosol indirect effect is caused by the influence of aerosols that change the cloud microphysical and optical properties, amount, and lifetime by acting as cloud condensation nuclei. There are still large uncertainties in the aerosol radiative forcing calculated by various global aerosol models that estimate the aerosol climate effects [*Schulz et al*., 2006; *IPCC*, 2007]. One of the uncertainties in the evaluated radiative forcing for the aerosol direct effect is the effect of vertical stratification of aerosols and clouds. Previous studies suggest that the direct aerosol radiative forcing (DARF) significantly depends on the amount of aerosols loaded above the cloud layer. In particular, absorbing aerosols as emitted from biomass burning above clouds produce a large positive forcing off southern Africa and South America [*Keil and Haywood*, 2003; *Takemura et al*., 2005]. *Haywood et al*. [2004] used measurements of the vertical profiles of aerosols and clouds off the coast of southern Africa from aircraft to demonstrate that MODIS retrievals exhibit a low bias in cloud optical depth and cloud effective radius. *De Graaf et al*. [2012] used data of passive satellite spectrometry from the ultraviolet to the shortwave infrared for estimating the aerosol solar absorption by the above-cloud aerosols. The cloud optical properties are retrieved using three channels in shortwave infrared for calculating the cloud reflectance in the modeled aerosol-free condition. DARF is estimated by the difference of the cloud reflectance between measurement and modeled aerosol-free calculation. They reported that DARF of the above-cloud absorbing aerosols off south Africa is +23 Wm^{-2} in August 2006.

[3] In April 2006, the Cloud-Aerosol Lidar and Infrared Pathfinder Satellite Observations (CALIPSO) satellite was launched with the space-borne lidar, CALIOP (the Cloud-Aerosol Lidar with Orthogonal Polarization), as one of the NASA Earth System Science Pathfinder (ESSP) programs. CALIOP, for the first time, provides us with global data of aerosol and cloud vertical profiles [*Winker et al*., 2009, 2010]. Clouds and aerosols are discriminated using a combination of 532 nm backscatter magnitude and attenuated color ratio,

[1]Atmosphere and Ocean Research Institute, University of Tokyo, Kashiwa, Japan.
[2]NASA Langley Research Center, Hampton, New Hampshire, USA.

Corresponding author: E. Oikawa, Atmosphere and Ocean Research Institute, University of Tokyo, 5-1-5 Kashiwanoha, Kashiwa, Chiba 277-8568, Japan. (e_oikawa@aori.u-tokyo.ac.jp)

2169-897X/13/10.1002/jgrd.50227

which is the ratio of 1064 and 532 nm of attenuated backscatter intensity [*Liu et al*., 2009]. The profiles of extinction coefficients for clouds and aerosols are retrieved from extinction retrieval algorithms [*Young and Vaughan*, 2009]. CALIOP can detect and retrieve aerosols above clouds [*Winker et al*., 2010]. These aerosols are unable to be detected from ground-based lidar measurements.

[4] *Chand et al*. [2009] evaluated the aerosol direct effect over the Atlantic Ocean off southwest Africa using aerosol optical thickness (AOT) of aerosols above low-level optically thick clouds quantified by retrieval methods of *Hu et al*. [2007] and *Chand et al*. [2008]. This paper reported that the DARF largely depends on the fractional coverage and albedo of the underlying clouds. Thus, cloud and aerosol profiling is significantly important for an accurate evaluation of the aerosol direct effect.

[5] We calculate the shortwave (SW) DARF of the total (natural plus anthropogenic) aerosols using aerosol and cloud distributions of both CALIOP observation and global aerosol modeling with the Spectral Radiation-Transport Model for Aerosol Species (SPRINTARS) [*Takemura et al*., 2000, 2002, 2005] for a year, 2007.

2. Data

[6] Monthly mean values of observation data and simulation results are used for calculating the SW DARF between 60°S and 60°N each month in 2007. Aerosol and cloud fields from 60°S to 60°N are obtained from CALIOP and Moderate Resolution Imaging Spectroradiometer (MODIS) sensors throughout the year. We needed to cut the high-latitude region off from our analysis, because we cannot get MODIS cloud optical thickness (COT), which is necessary for all-sky DARF calculation (section 3.2). We can explore higher latitudes up to 70°, but the sampling becomes uneven depending on the season and the resulting map may not be useful for the community. On the other hand, the model can compute DARF in any zone of the globe, and we omit the same high latitude for the sake of comparison with satellite values.

2.1. Data for the Observation DARF

[7] The CALIOP's laser produces linear polarized pulses at two wavelengths (532 nm and 1064 nm) from a near nadir-viewing geometry during both day and night phases of the orbit; after that, its receiver measures total backscattered intensity at 1064 nm, and two orthogonal polarized components at 532 nm.

[8] We use the CALIOP Level 2 Cloud and Aerosol Layer Products Version 2 (http:// eosweb.larc.nasa.gov/PRODOCS/calipso/table_calipso.html) of 5 km horizontal resolution. They provide the properties of the atmospheric features (e.g., cloud and aerosol layers). We use AOT at 532 nm, cloud optical thickness (COT), aerosol and cloud layer top and base altitudes, the cloud-aerosol discrimination (CAD) score, and the feature type of aerosols and clouds. The CAD Score, in the range between −100 and 100, is the value of quality assurance of discrimination between aerosol and cloud for each layer [*Liu et al*., 2009]. The atmospheric feature is classified as aerosol when the CAD score is negative, whereas it is classified as cloud when the score is positive. The higher the absolute value of CAD score, the more confident the classification of the feature is. The success ratio of classification of aerosols and clouds is larger than 90% and 83% of the classified aerosols, and 95% of the classified clouds have the absolute value CAD score, which is greater than 70 [*Liu et al*., 2009]. In this study, aerosol and cloud layers are defined when the absolute value of CAD score is higher than 70 for the quality assurance of the aerosol and cloud data. *Kittaka et al*. [2011] compare CALIPSO Version 2 AOT and Aqua MODIS Collection 5 AOT. The global mean of MODIS AOT which is collocated with CALIOP AOT is 0.08 to 0.12, depending on the cloud clearing applied. When the most stringent cloud clearing is used, the global means of collocated CALIPSO and MODIS AOT are in agreement, and the differences of AODs are 0.007 and 0.012 over ocean and land, respectively. However, it was found that CALIOP AOT is lower than MODIS AOT over China, Middle East, and Europe, and CALIOP AOT is higher than MODIS AOT over central and southern Africa.

[9] Aerosol layers in the CALIOP data files are classified as one of the six CALIOP aerosol types [*Omar et al*., 2009], while cloud layers are classified into two types: water or ice. The six CALIOP aerosol types are desert dust, smoke, clean continental, polluted continental, marine, and polluted dust. For computation of forcing from the CALIOP observations, refractive indices and size distributions of the six aerosol types of the CALIOP aerosol model [*Omar et al*., 2009] and cloud particles (water and ice) were used. The external mixture is assumed for each aerosol and cloud component. Single scattering albedo (SSA) of aerosol particles are calculated with reference to refractive indices and size distributions of aerosols of CALIOP model and SPRINTARS. Mean radius, geometric standard deviation (GSD), and calculated SSA of each aerosol component are listed in Table 1. The SSA derived from the CALIOP aerosol models is not always realistic. For example, the SSA of the clean continental model is smaller than that of polluted continental mode; that of the mineral dust aerosol model is smaller than recent reports from passive satellite remote sensing and ground-based measurements [*Kaufman et al*., 2001; *Dubovik et al*., 2002; *Yoshida and Murakami*, 2008]. Further, a fixed lidar ratio is assigned to each of the CALIOP aerosol models, so that the spatial and temporal variations of the aerosol components are not taken into account. These are the limitations of this type of lidar retrieval. If the value of the lidar ratio is not realistic, the estimated AOT will be incorrect. The SSA and asymmetry factor (g) may also have errors. The larger uncertainties will be caused by the increasing number of aerosol types to cover local variation of aerosols. It might be pointed out, however, that the error propagation to the evaluated DARF at TOA will be eased by the cancelation between errors in assumed aerosol optical properties and in retrieved lidar AOT. In case of overestimation of the aerosol imaginary index, then the AOT becomes overestimated, so that decreasing TOA DARF due to overestimated absorption effect and increasing TOA DARF due to overestimated AOT tend to cancel each other out. As far as we use the same CALIOP aerosol optical model in this study, the optical properties of the CALIOP product are consistent with the estimated TOA DARF through the radiative transfer calculation. If we use other aerosol optical models, we get rather larger errors in the DARF estimation because of the inconsistency of the

Table 1. Mean Radius, Geometric Standard Deviation (GSD), and Single Scattering Albedo (SSA) of the CALIOP Aerosol Model and SPRINTARS Aerosol Particles[a]

	CALIOP				SPRINTARS		
	Mean Radius (μm)	GSD	SSA (532 nm)		Mean Radius (μm)	GSD	SSA (550 nm)
Dust	0.1165 (f) 2.8329 (c)	1.4813 (f) 1.9078 (c)	0.92	Dust	4.0	2.5	0.91
Smoke	0.1436 (f) 3.726 (c)	1.5624 (f) 2.1426 (c)	0.83	BC	0.0499	2.0	0.17
Clean Continental	0.20556 (f) 2.6334 (c)	1.61 (f) 1.8987 (c)	0.90	OC	0.0282	1.8	1.00
Polluted Continental	0.1577 (f) 3.547 (c)	1.5257 (f) 2.065 (c)	0.93	Sea Salt	2.12	2.51	1.00
Clean Marine	0.150 (f) 1.216 (c)	1.600 (f) 1.600 (c)	0.99	Sulfate	0.313	2.03	1.00
Polluted Dust	0.1265 (f) 3.1617 (c)	1.5112 (f) 1.9942 (c)	0.85				

[a]The wavelength of SSA of CALIOP is 532 nm and that of SPRINTARS is 550 nm. The size distribution of CALIOP is the bimodal lognormal size distribution, which has fine mode (f) and coarse mode (c) [*Omar et al.*, 2009]. Mean radius of SPRINTARS is that of dry particle [*Takemura et al.*, 2005].

optical models used in the lidar retrieval and in the radiative transfer calculation. Therefore, we use the CALIOP aerosol model for our broadband radiative flux calculation for estimation of the DARF.

[10] Optically thick clouds with COT larger than about 3 completely attenuate the lidar beam; thus, the CALIOP lidar is unable to detect aerosols and clouds under the cloud top of an optically dense cloud layer. Instead, we use the COT derived by a passive satellite sensor, i.e., MODIS. The MODIS sensor, aboard the NASA Earth Observing System Terra and Aqua satellites, measures radiances in 36 channels including infrared and visible bands with spatial resolution between 250 m and 1 km. MODIS-derived COT in the MYD08_M3 product is applied to the CALIOP cloud profile when aerosols exist above clouds (above-cloud case) in the radiation calculation from observation (section 3.2). Previous studies reported that the aerosol absorption above clouds cause the underestimation of COT in the satellite retrievals [*Haywood et al.*, 2004; *Coddington et al.*, 2010]. In this study, we ignore this effect, because the underestimation of observed COT would not change our conclusions (section 4.1.2).

[11] In the analysis and radiation calculations, aerosol and cloud products are averaged to a horizontal resolution of $1^\circ \times 1^\circ$.

2.2. Data for the GCM Model DARF

[12] The aerosol radiation and transport model, SPRINTARS, is coupled with an atmospheric general circulation model (AGCM) of the Center for Climate System Research (CCSR), University of Tokyo, National Institute for Environmental Studies (NIES), and Frontier Research Center for Global Change (FRCGC) [*K*-1 *Model Developers*, 2004]. This AGCM is the atmospheric component of the Model for Interdisciplinary Research on Climate (MIROC) and has been contributing to various climate researches and assessments including the Intergovernmental Panel on Climate Change Fourth Assessment Report [e.g., *Lin et al.*, 2006]. MIROC-SPRINTARS calculates mass mixing ratios of the main tropospheric aerosols, that is, carbonaceous aerosol (black carbon (BC) and organic carbon (OC)), sulfate, soil dust, sea salt, and the precursor gases of sulfate (sulfur dioxide (SO2) and dimethylsulfide(DMS)) [*Takemura et al.*, 2000, 2002, 2005]. The aerosol transport processes include emission, advection, diffusion, sulfur chemistry, deposition, and gravitational settling. *Takemura et al.* [2002] reported that the simulated seasonal and geographical distribution patterns of aerosols are consistent with AVHRR retrievals. Seasonal mean biases of AOT are less than 30% at most AERONET sites. The time variation of the simulated Ångström exponent is consistent with AERONET results. The simulated SSA is lower than that of AERONET over the Saharan desert and higher than over industrial regions. Therefore, *Takemura et al.* [2005] used a quarter of the imaginary part for soil dust as proposed by *Deepak and Gerber* [1983] and calculated the direct and indirect effects of anthropogenic aerosols.

[13] In this study, aerosol emissions are the same as those in *Takemura et al.* [2005]. Model simulation is performed with a horizontal resolution of T42 (approximately $2.8^\circ \times 2.8^\circ$) with 20 vertical layers. The simulation is done for 1 year after 1 year spin-up with nudged meteorological fields (wind speed, water vapor, and temperature) of reanalysis data provided by the NCAR/NCEP. Sea surface temperature and sea ice distribution are fixed in this simulation to monthly means. Clear-sky AOT is defined as AOT when column cloud fraction is lower than 0.2. The column cloud fraction is calculated by the maximum random overlapping method at each time step in the model. AOT in all-sky condition $\tau_{\text{all-sky}}$ is calculated using clear-sky AOT $\tau_{\text{clear-sky}}$ and cloudy-sky AOT $\tau_{\text{cloudy-sky}}$ as follows:

$$\tau_{\text{all-sky}} = (1 - C)\cdot\tau_{\text{clear-sky}} + C\cdot\tau_{\text{cloudy-sky}}, \quad (1)$$

where C is the column cloud cover fraction. *Yu et al.* [2006] reported that the clear-sky AOT is smaller than all-sky AOT in both SPRINTARS and GISS models. Clouds can increase AOT through water uptake in the high humidity regions adjacent to clouds, but this cloud effect on AOT is model dependent.

[14] For SPRINTARS forcing, the refractive indices of aerosols and clouds depend on wavelength, size distribution, and hygroscopic growth of sulfate and carbonaceous aerosols.

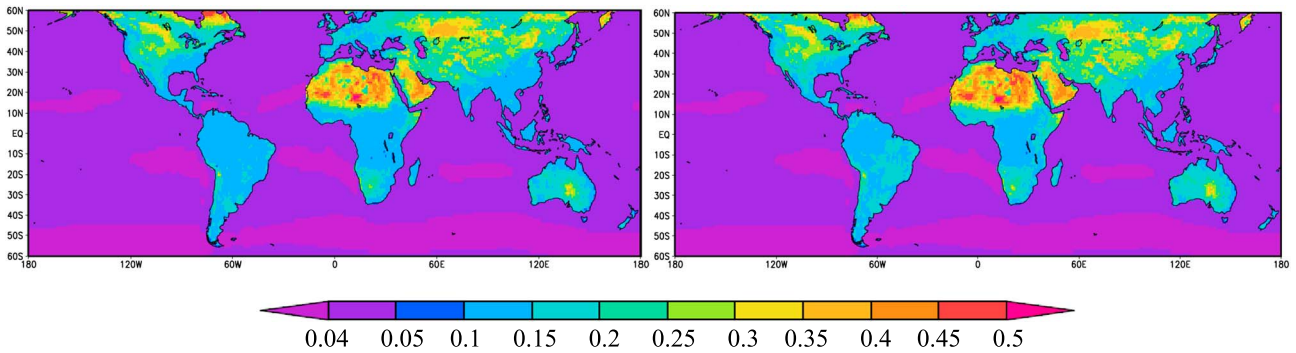

Figure 1. Annual mean distributions of the MODIS land surface albedo and sea surface albedo at 1° by 1°. Land surface albedos are for black-sky (left) and white-sky (right). Sea surface albedo is calculated by the FSTAR radiation code using NCEP surface wind velocity.

Refractive indices of dry aerosols and cloud particles (water and ice) are based on *Deepak and Gerber* [1983], *d'Almeida et al.* [1991], and *Sutherland and Khanna* [1991], except for the imaginary part of soil dust. The imaginary part of the refractive index of soil dust is a quarter of values as given by *Deepak and Gerber* [1983], because recent studies [e.g., *Kaufman et al.*, 2001, *Dubovik et al.*, 2002] indicated smaller value than that as given by *Deepak and Gerber* [1983] (Table 1). The fixed mode radius of each dry particle and standard deviation is based on the work of *Martins et al.* [1996] for carbonaceous aerosols and *d'Almeida et al.* [1991] for other aerosols. Carbonaceous aerosols are assumed as pure BC, pure OC and the internal mixture of BC and OC for the radiation transfer calculation. The hygroscopic growth of aerosol particles is according to *Tang and Munkelwitz* [1994] for sulfate and *Hobbs et al.* [1997] for carbonaceous particles. The detailed information is described in *Takemura et al.* [2005].

2.3. Common Data for Observation and Model DARF

[15] Surface albedo is one of the important parameters that changes the aerosol forcing at TOA [*Nakajima et al.*, 2007, *Kim and Ramanathan*, 2008]. The sensitivity of DARF to aerosol and cloud vertical distribution between observation and modeling are focused upon in this study, so that the MODIS surface albedo product, MCD43C3, is used in the radiative calculation for observation and simulation. MODIS provides surface albedo data in seven narrow bands and in three broadbands (visible, near infrared, and shortwave). MODIS global albedo data are at a 0.05° by 0.05° spatial resolution [*Schaaf et al.*, 2002; *Roesch et al.*, 2004]. The albedo products include black-sky and white-sky albedos for direct and diffuse beam, respectively. *Yu et al.* [2004] examined the dependence of the clear-sky DARF on black-sky and white-sky albedos. Their simulation assumption of DARF calculation uses the assumed fraction of direct beam, which is between 0 and 1, and AOT of 0.4 at 550 nm. This DARF is more close to the DARF using black-sky albedo than the DARF using white-sky albedo. The difference of DARF from using white-sky albedo is within 5%. Therefore, we use the black-sky albedo for clear-sky condition and the white-sky albedo for cloudy-sky condition. Surface albedo values for radiation calculation are interpolated from 0.3 to 4.0 μm using seven narrow bands and visible and near-infrared broadband land surface albedos of the MODIS product. Figure 1 shows the annual mean shortwave broadband surface albedos in 2007 at 1° by 1°. The white-sky albedo is larger than the black-sky albedo, except for evergreen broadleaf forest [*Gao et al.*, 2006]. The difference of white-sky albedo and black-sky albedo is about 0.01. Over central Eurasia around 50°N and North America, the seasonal variation is large, because of snow cover in winter and spring seasons. The ocean surface albedo is calculated by FSTAR radiation code in using the surface wind velocity of NCEP/NCAR reanalysis data [*Kalnay et al.*, 1996]. The ocean surface albedo is assumed to be dependent on the surface wind velocity [*Nakajima and Tanaka*, 1983]; the ocean surface albedo decrease with increasing the wind velocity. The surface albedo is about 0.05 over most part of the ocean, except for the mid-latitude ocean from 50°S to 60°S latitude, where the wind velocity is more than 10 m s^{-1}.

[16] NCEP/NCAR meteorological data (pressure, temperature, and specific humidity) are used for constructing the model atmosphere for radiative transfer computation.

[17] These data are interpolated onto a horizontal resolution of 1° × 1° and T42 (approximately 2.8° × 2.8°) for the observation and the model results, respectively.

3. Model Description of Radiative Calculation

3.1. Radiation Code

[18] A radiative transfer code FSTAR5c is a flux version of the System of Transfer of Atmospheric Radiation (STAR) [*Ruggaber et al.*, 1994]. The FSTAR model calculates radiative fluxes with a range from 0.2 to 200 μm using a four-stream flux approximation under the plane-parallel layers with water vapor and other trace gases, various types of aerosol and cloud polydispersions, and ground/ocean surfaces with radiative transfer algorithms of *Nakajima and Tanaka* [1983, 1986, 1988] (OpenCLASTR http://www.ccsr.u-tokyo.ac.jp/~clastr/).

[19] We performed 40 band calculations from 0.3 to 4 μm for monthly averaged broadband shortwave DARF. The three-term *k*-distribution method of AFGL/Lowtran [*Kneizys et al.*, 1988] is used for gaseous absorption. This calculation is performed every 1 h using solar zenith angles on the 15th

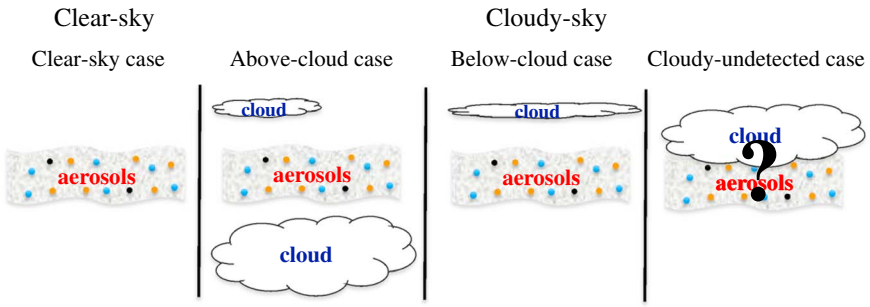

Figure 2. Four scenarios for radiation calculation: clear-sky (left) and cloudy-sky conditions with cases of aerosols existing above clouds (left-middle), below high clouds such as cirrus (right-middle) but without clouds below the aerosol layers, and aerosols not observed in cloudy-sky condition (right). Above-cloud case (left-middle) is the case that aerosols exist above low-level clouds, with or without high-level clouds. Cloudy-undetected case (right) is the case that aerosols that exist below or within optically thick clouds are not detected by the satellite lidar.

of each month. The vertical resolutions of radiation calculation are 0.5 km from ground surface to 5 km altitude, 1 km from 5 km to 25 km altitude, and 2.5 km from 25 km to 40 km. The observation and model data are interpolated onto these vertical resolutions in the radiation calculation.

3.2. Method of DARF Calculation

[20] We calculated the monthly mean value of the SW DARF at the top of the atmosphere (TOA) under clear-sky and cloudy-sky conditions using the observation data and simulation results. High cloud reflectance changes the DARF from negative to positive [*Haywood and Shine*, 1997]. Hence, we made two scenarios under cloudy-sky condition: one is the case of aerosols existing above clouds (above-cloud case) and the other is the case of aerosols existing below high clouds such as cirrus (below-cloud case) but without clouds below the significant aerosol layers. We decided that the above-cloud scenario also includes the case of aerosol layers with low-level clouds and high-level clouds existing at the same time, because high-level clouds decrease the absolute value of aerosol radiative effect but do not change its sign.

[21] Aerosols widely exist from surface to the upper troposphere and are mixed with clouds. Nevertheless, the CALIOP lidar is unable to detect aerosols under optically thick clouds, because the limitation of optical thickness by CALIOP is about 3. The aerosols undetected by CALIOP sensor exist below/within the optically thick clouds. We define this case as the cloudy-undetected scenario. In this study, we assume the DARF of the cloudy-undetected case is close to zero, because optically thick clouds dominantly scatter the incident sunlight.

[22] The above-mentioned four scenarios are schematically illustrated in Figure 2. The cloudy-sky forcing is the combination of aerosol radiative forcings in above-cloud and below-cloud cases in proportion to the occurrence probability of each case. The all-sky forcing is the combination of clear-sky forcing and cloudy-sky forcing with weights of the cloud cover fraction. The details of this computation method are described in section A. Figure 3 shows the occurrence probabilities of four scenarios. The pattern of occurrence probability of the clear-sky case is similar, but the value of the model is higher than that of the observation. CALIOP observes optically thin clouds that are undetected in the ISCCP product [*Winker et al.*, 2010]. Off southern Africa, the probability that aerosols are observed above clouds is about 0.5, but less cloud is simulated in the model and the occurrence probability of the clear-sky case is about 0.7. Over land, aerosols hardly exist above clouds in both the observation and the model. Over the Pacific and the central Africa, aerosols exist below clouds in both the observation and the model. The probability of the observation is lower than that of the model, because the aerosols that exist below/within the optically thick clouds are undetected by CALIOP. The occurrence probability of cloudy-undetected case is the largest in four scenarios, and a large amount of aerosols are not detected in cloudy-sky condition. Over the ocean around 60°S, aerosols are hardly observed by CALIOP, because optically thick clouds usually exist.

[23] The procedure of the separation of the above-mentioned four scenarios for CALIOP data is described below. At first, we examine whether aerosol layers and/or cloud layers exist for each 5 km product. If only aerosol layers exist, we define that this case is the clear-sky scenario. If the base altitude of the lowest aerosol layer is higher than that of the lowest cloud layer, we define this case as the above-cloud scenario. In this case, aerosols usually exist above low-level clouds. If the base altitude of the lowest aerosol layer is lower than that of the lowest cloud layer, we define this case as below-cloud scenario. In this case, aerosols usually exist below high clouds such as cirrus. The mixed layer of aerosols and clouds are included in the above-cloud case and below-cloud case, due to the definition of each scenario. Each aerosol layer is classified for one of the six aerosol types, and each cloud layer is classified for water or ice by CALIOP algorithm. The column AOT of aerosol type, COT of water and ice, and profile information of aerosols and clouds for each scenario are aggregated and averaged at 1° by 1° horizontal resolution every month in 2007.

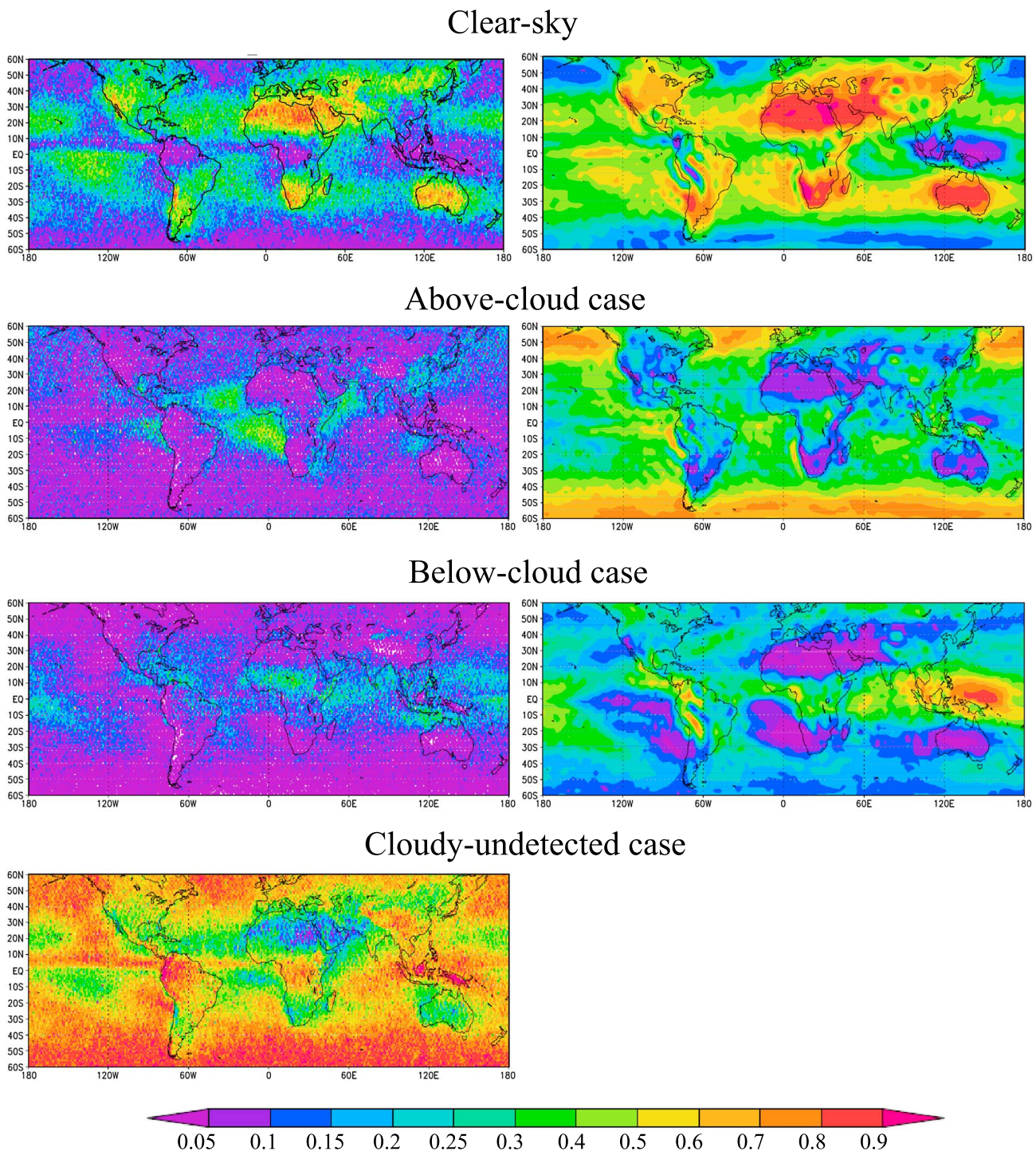

Figure 3. Occurrence probabilities of four scenarios (clear-sky, above-cloud, below-cloud, and cloudy-undetected cases). Occurrence probability of SPRINTARS in cloudy-undetected case is zero, because aerosols are simulated below or within optically thick clouds in SPRINTARS.

[24] The AOT above the cloud height of the MODIS product is obtained from the CALIOP Product. MODIS-derived COT, $\tau_{\text{cloud, MODIS}}$, is applied for the CALIOP cloud profile when aerosols exist above clouds (above-cloud) in radiation calculation for the observation. CALIOP COT, $\tau_{\text{cloud, CALIOP}}$, is sum of the CALIOP COT below the MODIS cloud top, $\tau_{\text{low-cloud, CALIOP}}$, and CALIOP COT above the MODIS cloud top, $\tau_{\text{high-cloud, CALIOP}}$:

$$\tau_{\text{cloud,CALIOP}} = \tau_{\text{low-cloud,CALIOP}} + \tau_{\text{high-cloud,CALIOP}}. \quad (2)$$

The profile of extinction coefficient for cloud particles is the

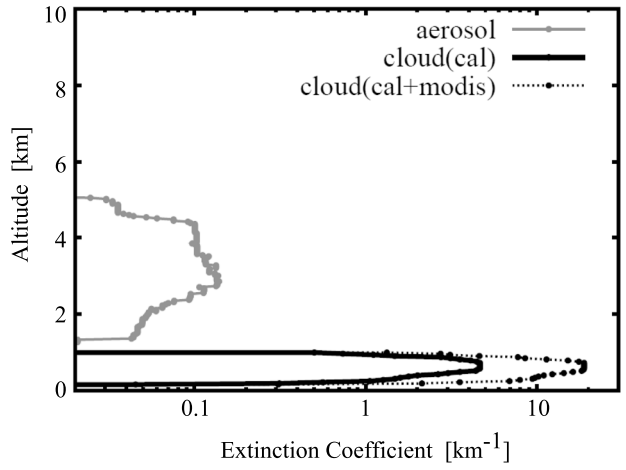

Figure 4. The monthly mean profile of extinction coefficient for aerosols and clouds observed by CALIOP at above-cloud case at grid point (15°S, 5°E) in September 2007. Two cloud profiles are shown: one is CALIOP observed profile and the other is the CALIOP profile applied with MODIS COT. The x axis shows the logarithmic scale of the extinction coefficient [km^{-1}] and the y axis shows the altitude [km].

extinction profile observed by CALIOP multiplied by the scaled factor $(\tau_{\text{cloud,MODIS}} - \tau_{\text{high-cloud,CALIOP}})/\tau_{\text{low-cloud,CALIOP}}$ below the MODIS cloud top:

$$\sigma_{\text{cloud}}(z) = \frac{\tau_{\text{cloud,MODIS}} - \tau_{\text{high-cloud,CALIOP}}}{\tau_{\text{low-cloud,CALIOP}}} \times \sigma_{\text{cloud,CALIOP}}(z), \tag{3}$$

where $\sigma_{\text{cloud}}(z)$ is the extinction coefficient of clouds in the above-cloud case and $\sigma_{\text{cloud,CALIOP}}(z)$ is the extinction coefficient observed by CALIOP at each altitude. Figure 4 shows the monthly mean profile of extinction coefficient for aerosols and clouds observed by CALIOP at above-cloud case at grid point (15°S, 5°E) in September 2007. The aerosol layer exists from 1.5 to 5 km altitude, and the cloud layer exists below 1.5 km. Two cloud profiles of the extinction coefficient, $\sigma_{\text{cloud,CALIOP}}$ and σ_{cloud}, are shown. The cloud layer exist below 1 km altitude, and the maximum value of σ becomes about 20 by applying the MODIS COT. Although we may overestimate the bottom height of the cloud layer by the above-mentioned method, we do not think that this overestimation will cause a large error in the evaluated TOA flux as far as we suitably assume the value of COT by MODIS retrieval.

[25] For calculating the model DARF, aerosol distributions under clear-sky and all-sky conditions and cloud distribution are simulated from MIROC-SPRINTARS. The cloudy-sky aerosol distribution is obtained from simulated values under clear-sky and all-sky conditions, and the cloudy-sky AOT is used in the above-cloud case and the below-cloud case. To separate the simulated clouds in the above-cloud case and the below-cloud case, we used the approximation method of the homogeneous layers using the extinction coefficient profiles. In this analysis, aerosols and clouds were approximated as a system of multiple homogeneous layers through the analysis of vertical profiles of extinction coefficients of aerosols and clouds in order to quantify the layer parameters such as bottom and top altitudes of the layer. The high-level cloud layer is first classified as a cloud layer above the significant aerosol layers (below-cloud case), and then the rest of the clouds are classified as low-level clouds (above-cloud case) for the radiation calculation. Detailed aerosol and cloud stratification analysis is given elsewhere (Oikawa et al., in preparation, 2012).

4. Results

[26] Figure 5 shows the annual mean AOT distribution from 60°S to 60°N for each scenario. The wavelength of AOT is 532 nm for CALIOP and 550 nm for SPRINTARS. In CALIOP cases, the AOTs in the above-cloud and below-cloud cases are larger than that of the clear-sky case. Figure 6 shows the longitudinal mean CALIOP AOT in 2007 from 60°S to 60°N. It is found that the above-cloud and below-cloud AOTs are higher than the clear-sky AOT every latitude zone. In clear-sky and above-cloud cases, the peak of AOT is at around 10°N and AOT decreases with increasing latitude, except for the latitudinal zone from 0°N to 10°N. By contrast, the below-cloud AOT increases with increasing latitude, except for the latitudinal zone from 0°N to 20°S. In general, AOT over high latitude is smaller than that over low latitude, because the higher latitude, the farther from the emission of aerosols. It is assumed that the high below-cloud AOT over high-latitude zone is caused by misclassification of the optically thin low-level clouds as aerosols [*Liu et al*., 2009]. We need further studies to understand the reason of larger AOTs in cloudy cases in the CALIPSO product. The occurrence probability of the above-cloud and below-cloud cases is smaller than that of the clear-sky case; therefore, the cloudy-sky AOT of CALIOP is smaller than SPRINTARS AOT. In the SPRINTARS model cases, the cloudy-sky AOT is above 0.8 over East Asia, which is several tens of percentage larger than the clear-sky AOT, because of aerosol particle growth in a high relative humidity in the cloudy condition [*Yu et al*., 2006]. This cloud effect on increasing AOT is model dependent and should be studied more carefully in the future, because the interstitial aerosol concentration in the cloudy atmospheric column is also strongly dependent on the aerosol scavenging and washout effects. It is not possible to validate this point by the CALIOP observation because the lidar cannot observe the AOT in and below thick cloud layers.

[27] Figure 7 shows seasonal mean distributions of the SSA of aerosols from 60°S to 60°N. The wavelength of SSA is 532 nm for CALIOP and 550 nm for SPRINTARS. In southern Africa and South America, biomass burning aerosols are emitted in summer and autumn, the observation SSA is 0.84, and the model one is smaller than 0.8. In the observation and model, SSA is about 0.90 over desert regions. Over the pristine ocean, the model SSA becomes 0.96, while the observation value is a little smaller. In winter, low SSA is caused by biomass burning aerosols in central Africa. This is not significant in the observation result.

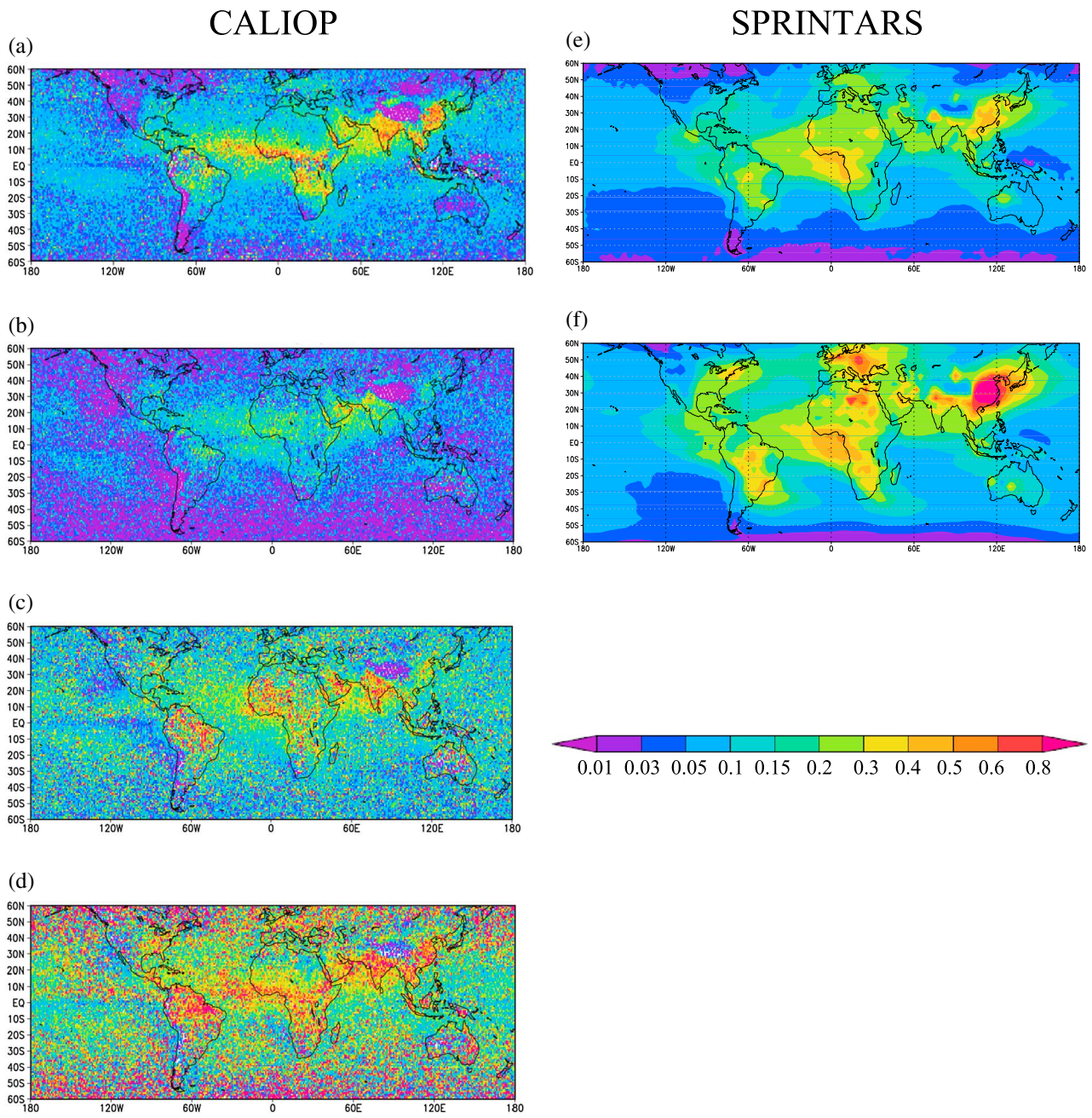

Figure 5. Annual mean distributions of AOT at 532 nm for clear-sky (a), cloudy-sky (b), above-cloud (c), and below-cloud (d) cases for CALIOP observation, and that of 550 nm for clear-sky (e) and cloudy-sky (f) cases for SPRINTARS simulation.

4.1. DARF at the TOA

4.1.1. Clear-Sky Condition

[28] Figure 8 shows seasonal mean distributions of SW DARF under clear-sky condition in the region of 60°S to 60°N from the observation and modeling. The absolute value of DARF is approximately proportional to AOT, but the magnitude and sign of the radiative forcing efficiency, defined as β = DARF/AOT, are determined by the single scattering albedo, asymmetry factor, and underlying surface albedo [*Fraser and Kaufman*, 1985; *Nakajima et al.*, 2007]. Over the Saharan and Arabian deserts, the DARF becomes positive by the high surface albedo and low SSA of dust particles in both observation and modeling. The model-simulated DARF is larger than that of observation. SSA of the model is as large as that of the observation, about 0.92, and the shortwave surface albedos are about 0.4, but AOT of the model is about two times larger than that of the observation. Thus, DARF of the model is more positive than that of the observation. The land surface has highly anisotropic and wavelength-dependent optical properties. This characteristic of surface albedo leads to the uncertainty of the estimation of DARF [*Yu et al.*, 2006], and we need to carry out future studies to narrow the uncertainty. In winter

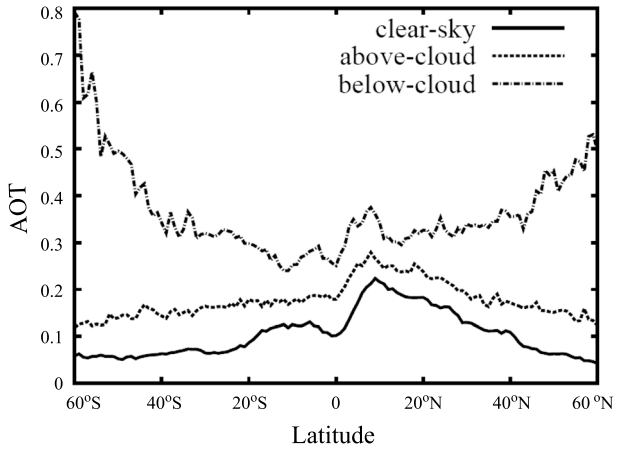

Figure 6. The longitudinal mean CALIOP AOT in 2007 from 60°S to 60°N in the clear-sky, below-cloud, and above-cloud cases.

and spring, DARFs over Russia, United States, and Canada show a small positive value of about +0.5 Wm^{-2} due to the bright snow and ice surface.

4.1.2. Above-Cloud Case

[29] Figure 9b shows the seasonal mean extinction profiles for aerosols and clouds of CALIOP and SPRINTARS in the above-cloud and below-cloud cases in the six selected areas (Figure 9a) in summer and autumn seasons. MODIS COT is applied for the cloud profile of CALIOP in the above-cloud case (section 3.2). The figure shows that the lidar-observed and model-simulated vertical profiles of aerosol and cloud layers are similar to each other with some higher-scale height of the cloud layers especially over China and South Africa. The model depicts the observed aerosol stratification fairly well. The heights of aerosol and cloud layers are different in each CALIOP observation. In the above-cloud case, the detection of aerosol layer decreases close to sea level, because the detection of cloud layer increases. Therefore, the extinction coefficient of aerosols decreases with increasing the extinction coefficient of clouds below 1 km altitude in the CALIOP above-cloud case.

[30] Figure 10 shows annual mean distributions of DARF and COT in the above-cloud case. Above-cloud DARF is positive over most parts of the globe in both observation and modeling. This point is significant, because most of the past studies reported positive DARF values in the above-cloud condition over limited areas, for example, off southern Africa [*Keil and Haywood*, 2003; *Chand et al*., 2009; *De Graaf et al*., 2012]. DARF values off southern Africa and over East Asia are more than +7 Wm^{-2}. Off southern Africa, low-level clouds exist below 2 km altitude and aerosols exist below 6 km altitude (Figure 9b, a3) and SSA is 0.84 in summer and autumn. Over China, aerosols exist below 6 km altitude within clouds (Figure 9b, a2) and SSA is about 0.86. In these regions, absorbing aerosols emitted from biomass burning and air pollution are loaded above or within low-level clouds and cause an enhanced absorption because of multiple scattering between aerosol and cloud layers [*Haywood and Shine*, 1997; *Takemura et al*., 2005]. In East Asia, the model DARF is more positive than the observation one, because the model AOT is twice as large as the observed AOT. *Koch et al*. [2009] reported that BC surface concentration of SPRINTARS agrees with the observed one over southeastern Asia, but it is overestimated in other regions. In this study, the dense aerosols are simulated around the surface over China. Previous studies reported that the absorbing aerosols above clouds bias the cloud satellite retrieval to less COT and smaller effective radius [*Haywood et al*., 2004; *Coddington et al*., 2010]. COT of the CALIOP and MODIS products is more than 7 over most regions (Figure 10); therefore, we assume that the underestimation of COT only slightly influences the DARF estimation. In the model, the DARF is negative or slightly positive over Eastern Europe, Central Eurasia, Western America, and Western Australia, whereas CALIOP-DARF is mostly positive in these regions. It is found from the detailed investigation of the model results that sulfate aerosols are the primary species and cause a large negative forcing over east Europe. The model SSA is 0.96, while that of the observation is 0.88 and positive forcing is caused in this region. Over Central Eurasia, Western America, and Western Australia, SSA is about 0.88, but COT is smaller than 2, so that the cloud effect is weak and aerosols indicate negative forcing.

4.1.3. Below-Cloud Case

[31] Annual mean distributions of DARF and COT in the below-cloud case are shown in Figure 11. In the observation, the pattern of DARF is similar to that of clear-sky DARF. The below-cloud forcing is larger than the clear-sky forcing because AOT observed in the below-cloud case is 3 times larger than clear-sky AOT (Figure 5 and Table 2). The radiative forcing efficiency in the below-cloud case is lower than that in the clear-sky case. The high-level clouds attenuate scattered light from the lower aerosol layers, so that TOA forcing and the radiative forcing efficiency is lower than the clear-sky situation. On the other hand, the DARF in the modeling has large differences from that in the clear-sky condition and even changes its sign over continental areas. The COT from CALIOP observation is smaller than 2. In contrast, the COT in the model is larger than 5. CALIOP only retrieves COT less than about 3; thus, the situation where the COT is larger than 3 is regarded as the cloudy-undetected case in CALIOP. Therefore, the pattern of DARF is different between the observation and the model. Over the regions where the COT is lower than 3, DARF is negative in both the observation and the model, except for the desert areas. In South America, DARF of CALIOP is negative, while DARF of SPRINTARS is positive. In Figure 9b, b2, aerosols exist below 6 km altitude in the observation and the model. Aerosols and optically thin clouds coexist in the observation, while aerosols exist within optically thicker clouds above 2 km altitude in the model. The light scattered by aerosols reaches to the TOA after attenuation by the higher-level clouds and the low SSA causes positive forcing in the model. Over the North Atlantic, the vertical distribution of aerosols and clouds is similar (Figure 9b, b1). Though the model SSA is higher than the observation, simulated dense clouds largely attenuate scattered light from the

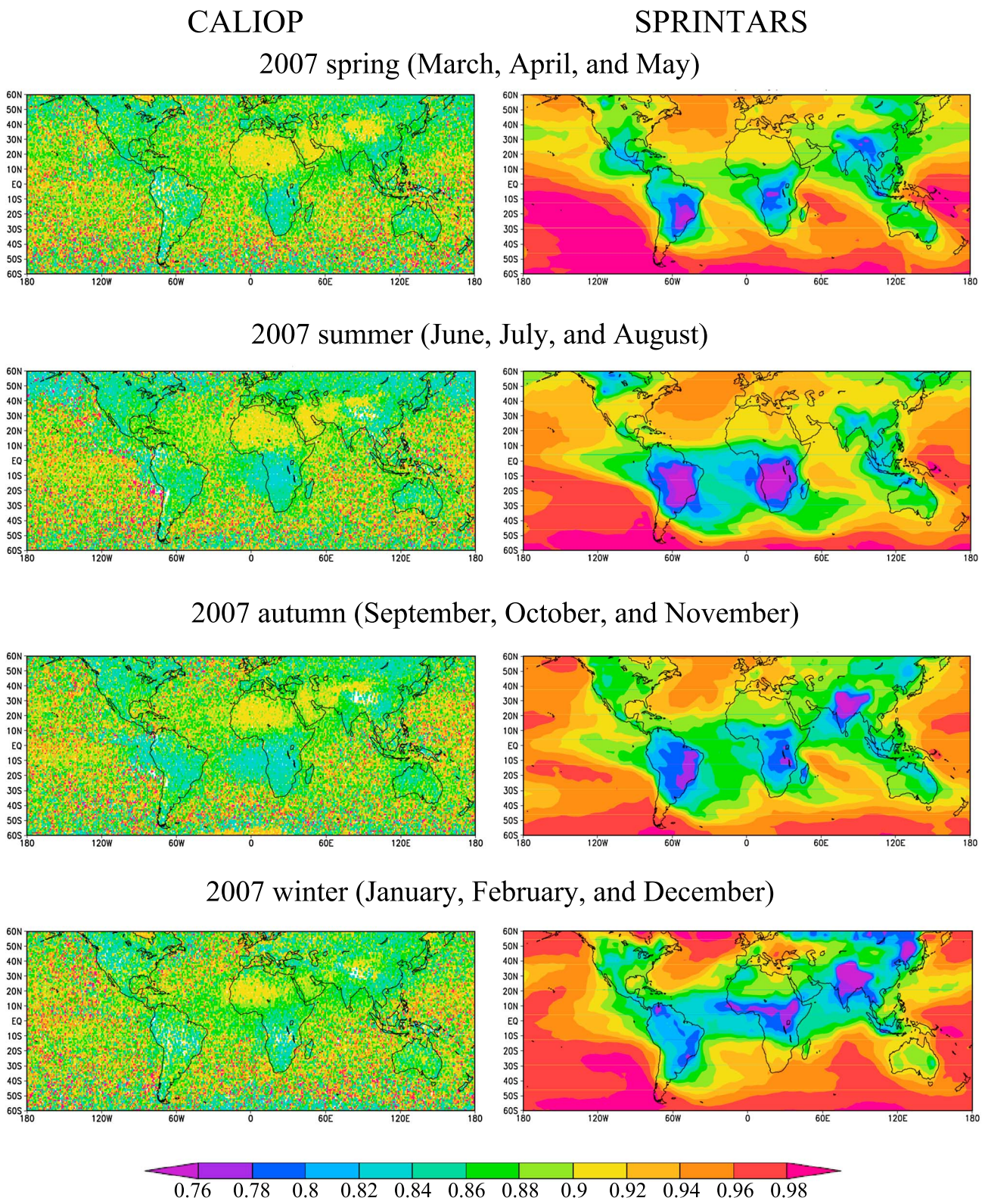

Figure 7. Seasonal mean distributions of the single scattering albedo for all-sky condition at 532 nm for the CALIOP observation (left) and at 550 nm for SPRINTARS (right).

lower layers. In addition AOT in the model is smaller than the observation so that it causes less negative forcing over dark surfaces in the Atlantic and Pacific oceans. In the above-cloud case, DARF is positive and aerosols exist within optically thick clouds in these regions (Figure 9b, a1 and a4). Though we use the same distributions and optical properties of aerosols in the model in the above-cloud and below-cloud cases, the sign of DARF

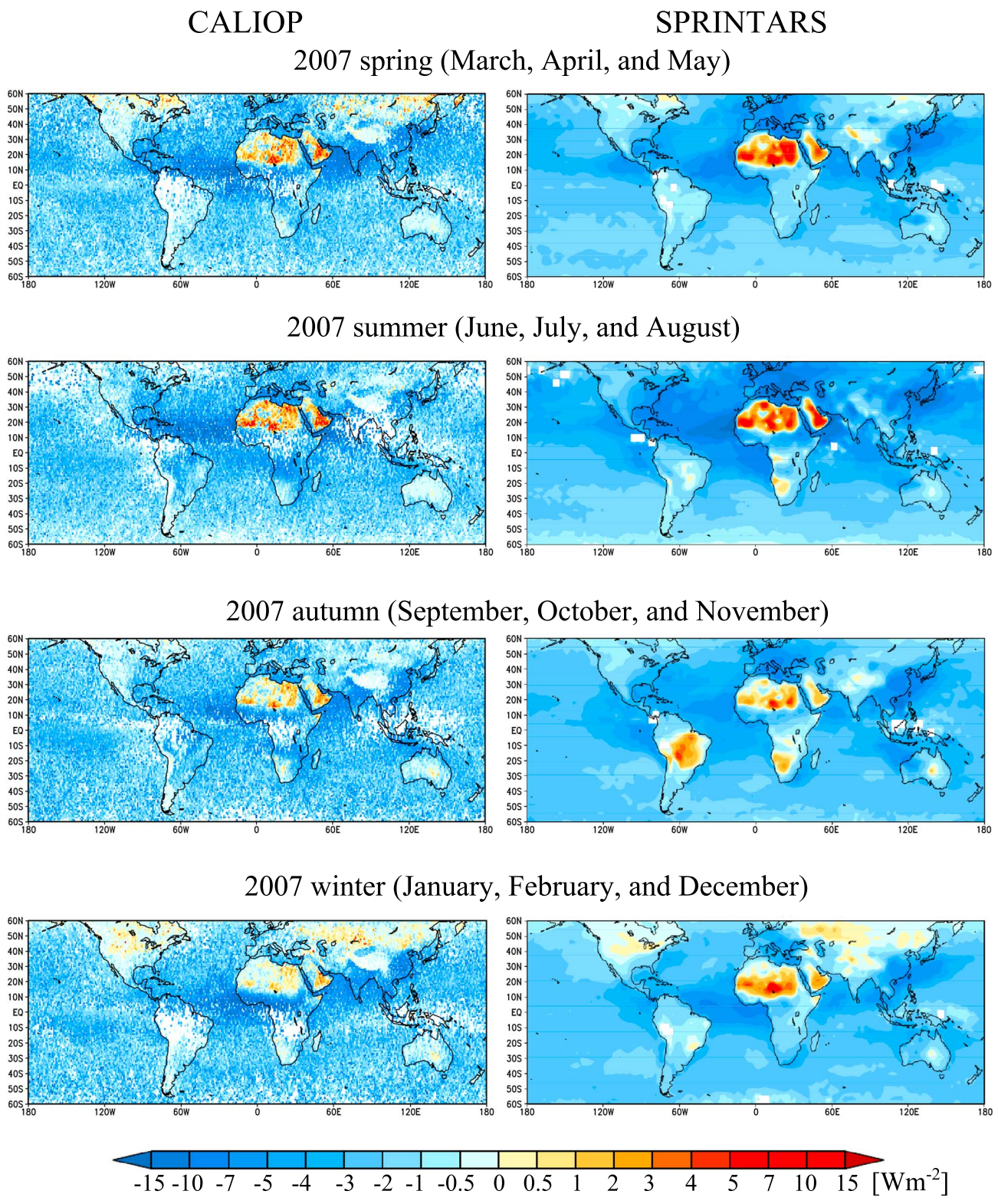

Figure 8. Seasonal mean distributions of the SW DARF for clear-sky case from the CALIOP observation (left) and simulated results by SPRINTARS (right).

is different between the above-cloud case and the below-cloud case. This indicates that aerosols within optically thick clouds cause positive forcing in our radiative transfer calculation, regardless of SSA.

4.1.4. Cloudy-Sky Condition

[32] Figure 12 shows seasonal mean distributions of the cloudy-sky DARF, $DARF_{\text{cloudy-sky}}$, which is the weighted means of forcings in the above-cloud, below-cloud, and

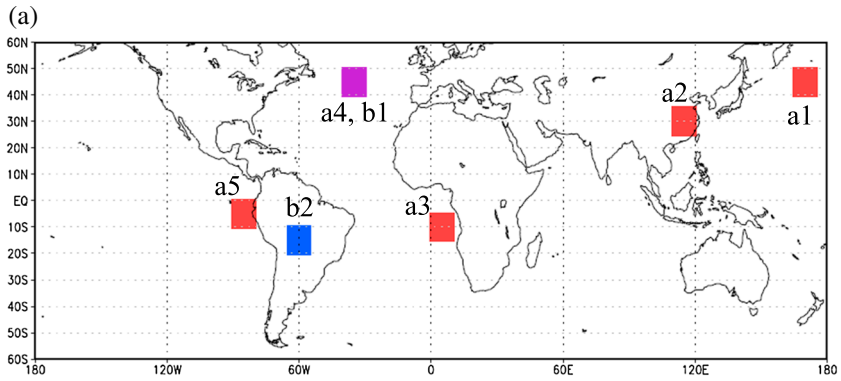

Figure 9. (a) Illustration of six sections selected for the comparison of the aerosol and cloud profiles in above-cloud and below-cloud cases. One section covers 10° by 10°, and the seasonal mean profiles of aerosols and clouds are averaged in this region. This analysis is performed in the above-cloud case (a1, a2, a3, and a5) at red grid boxes, in the below-cloud case (b2) at a blue-box and in the above-cloud (a4) and below-cloud (b1) cases at purple grid box. (b) The seasonal mean extinction profiles for aerosols and clouds of CALIOP and SPRINTARS in the above-cloud and below-cloud cases. MODIS COT is applied for the cloud profile of CALIOP in the above-cloud case (section 3.2). These profiles are averaged in the six sections (Figure 9a) in JJA and SON. The x axis shows the logarithmic scale of the extinction coefficient [km^{-1}] and the y axis shows the altitude [km].

cloudy-undetected cases with weights of occurrence probabilities in the three cases:

$$DARF_{\text{cloudy-sky}} = \sum_{i=ac,bc,uc} P_i \times DARF_i \approx \sum_{i=ac,bc} P_i \times DARF_i + 0 = \sum_{i=ac,bc} P_i \times DARF_i, \quad (4)$$

where P_{ac} is the probability of the above-cloud case, P_{bc} is that of the below-cloud case, and P_{uc} is that of the cloudy-undetected case:

$$P_{ac} = \frac{N_{ac}}{N_{\text{cloudy-sky}}}, \quad P_{bc} = \frac{N_{bc}}{N_{\text{cloudy-sky}}}, \quad \text{and} \quad (5)$$

$$P_{uc} = \frac{N_{\text{cloudy-sky}} - N_{ac} - N_{bc}}{N_{\text{cloudy-sky}}},$$

$$P_{ac} + P_{bc} + P_{uc} = 1, \quad (6)$$

where N_{ac}, N_{bc}, and $N_{\text{cloudy-sky}}$ are the pixel counts of above-cloud, below-cloud, and cloudy-sky cases, respectively. $DARF_{ac}$, $DARF_{bc}$, and $DARF_{uc}$ are DARF for above-cloud, below-cloud, and cloudy-undetected cases, respectively. In this study, $DARF_{uc}$ is assumed as zero, because optically thick clouds dominantly scatter the incident sunlight and the absorption by aerosols that exist within thick clouds cancels aerosol scattering. The CALIOP AOTs and DARFs in the above-cloud and below-cloud cases are more than 2 times larger than those of SPRINTARS, while the occurrence probabilities of CALIOP are less than half of SPRINTARS ones. Thus, the cloudy-sky AOT and DARF of CALIOP are smaller than SPRINTARS results. Aerosols are simulated below and within optically thick clouds in SPRINTARS; hence, P_{uc} is equal to zero for SPRINTARS.

[33] Areas of large positive forcings, above +5 Wm^{-2} correspond to the source and outflow regions of smoke from biomass burning and air pollution. Carbonaceous and dust aerosols emitted from East Asia cause a large positive forcing throughout the year. In particular, they are transported to the North Pacific and produce a positive forcing as large as +7 Wm^{-2} in the model in the summer season. Optically thick clouds remain below 2 km altitude, and aerosols are vertically distributed to 5 km altitude (Figure 9b, a1). SSA is 0.90 and DARF becomes large positive. In autumn, aerosols remain at lower altitudes and the column AOT is smaller, so that aerosols cause weaker positive forcing.

[34] Off South America, SPRINTARS-DARF is large positive in summer and autumn, while CALIOP-DARF is the largest positive in autumn season. The observed AOT is smaller than the simulated AOT, and aerosols in particular are hardly detected by CALIOP in autumn (Figure 9b, a5). In SPRINTARS, the emission inventories of carbonaceous aerosols originating from biomass burning, biofuel, agricultural activity, and fossil fuels are based on several databases from the Food and Agriculture Organization of the United Nations (FAO), Global Emissions Inventory Activities (GEIA), and energy statistics in each nation [*Takemura et al.*, 2005]. These emission inventories are not based on the observed fire hot spot counts and do not correspond to individual fire events. Hence, it is possible that the difference of DARFs between the observation and model is due to these emission inventory datasets. Similarly, smoke from South America is transported to the southern part of the Atlantic and causes a large positive forcing in the model, but its effect is quite small in the CALIOP result. We found that this difference is caused by an overestimation of AOT by model and/or underestimation of AOT by lidar observation.

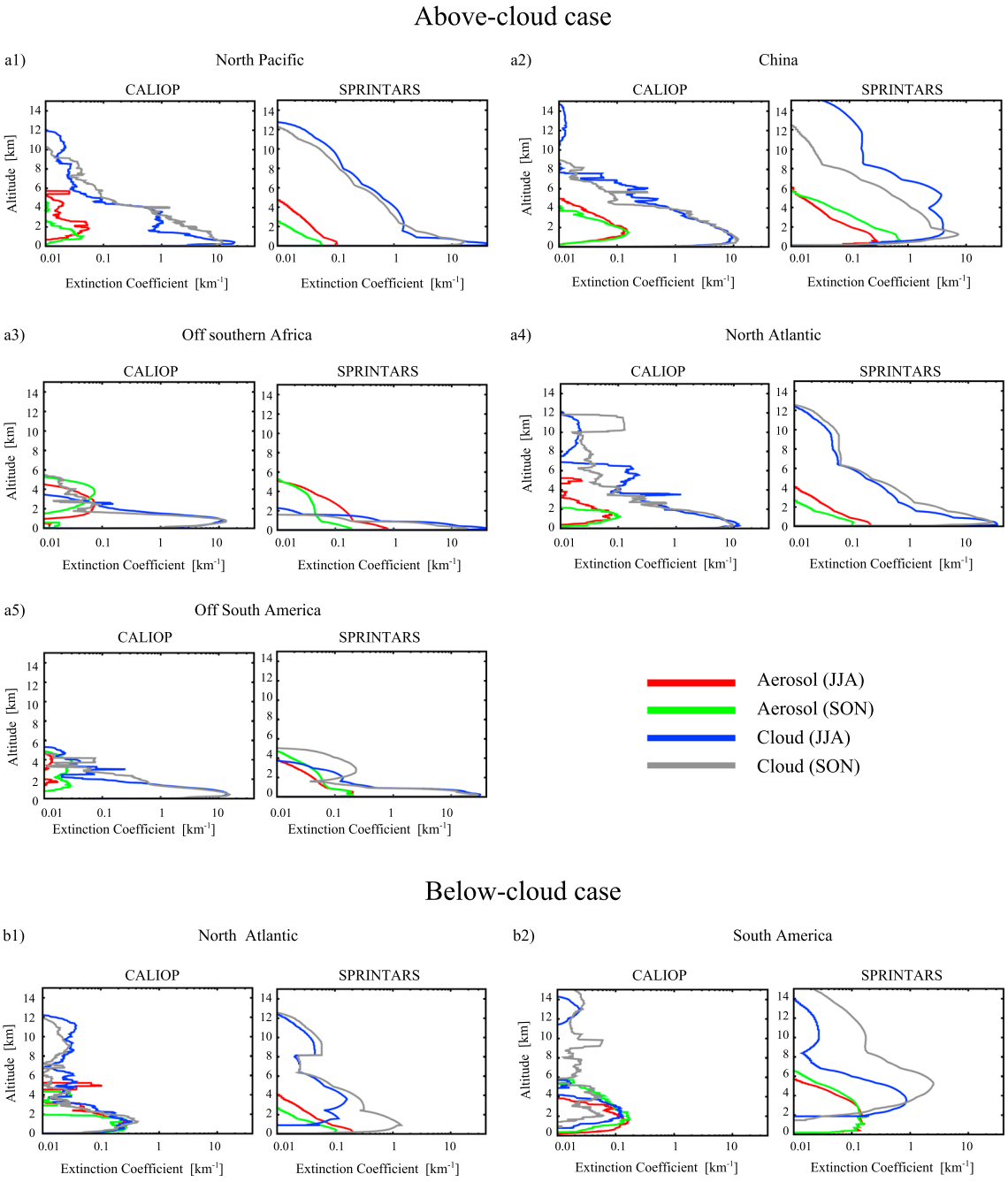

Figure 9. (continued)

Large AOT and low SSA cause larger positive forcing than that of CALIOP.

4.1.5. All-Sky DARF

[35] Figure 13 shows seasonal mean distributions of the all-sky DARF, $DARF_{\text{all-sky}}$, which is the combination of the clear-sky and cloudy-sky forcings in a similar way to the cloudy-sky forcing calculation;

$$DARF_{\text{all-sky}} = P_{\text{clear-sky}} \times DARF_{\text{clear-sky}} + P_{\text{cloudy-sky}} \times DARF_{\text{cloudy-sky}}, \quad (7)$$

where $P_{\text{clear-sky}}$ is the probability of clear-sky condition and $P_{\text{cloudy-sky}}$ is that of cloudy-sky condition.

[36] It is found from the figure that the all-sky forcing is negative over the ocean, except for outflow regions of smoke aerosols. The absorption over the desert regions occurs depending on the presence or absence of clouds. The column and high-level cloud cover fractions of the CALIOP product are above 0.8 and 0.5, respectively, over a large fraction of the ocean [*Winker et al.*, 2010]. The occurrence probability of CALIOP in clear-sky is smaller than the model, in contrast, so that the forcing of the modeling is more negative than the observation. This indicates that all-sky forcing largely depends on the cloud fraction [*Chand et al.*, 2009]. The DARF over Indonesia is negative or less positive from the observation, but it reaches +3 Wm^{-2} in the model. The

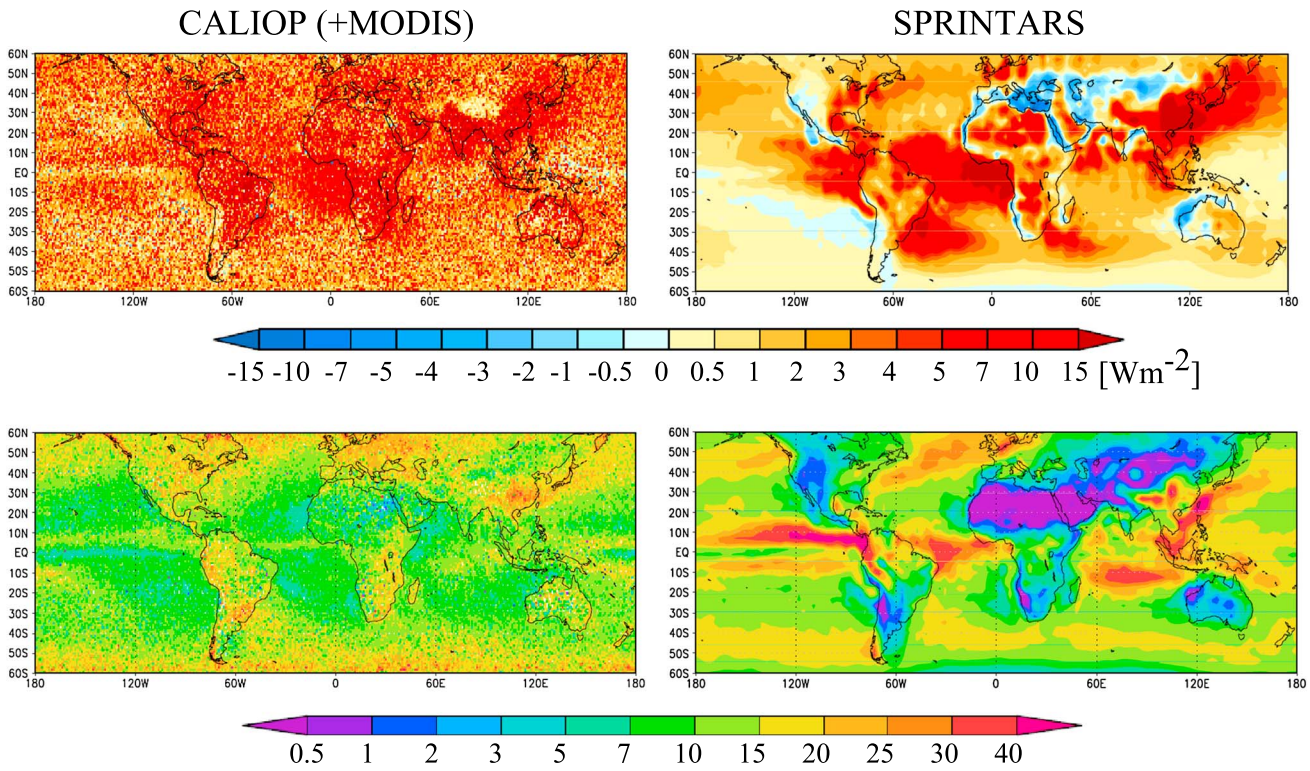

Figure 10. Annual mean distributions of SW DARF(top), and COT(bottom) of the above-cloud case from CALIOP and MODIS observation (left), and simulated results by SPRINTARS (right).

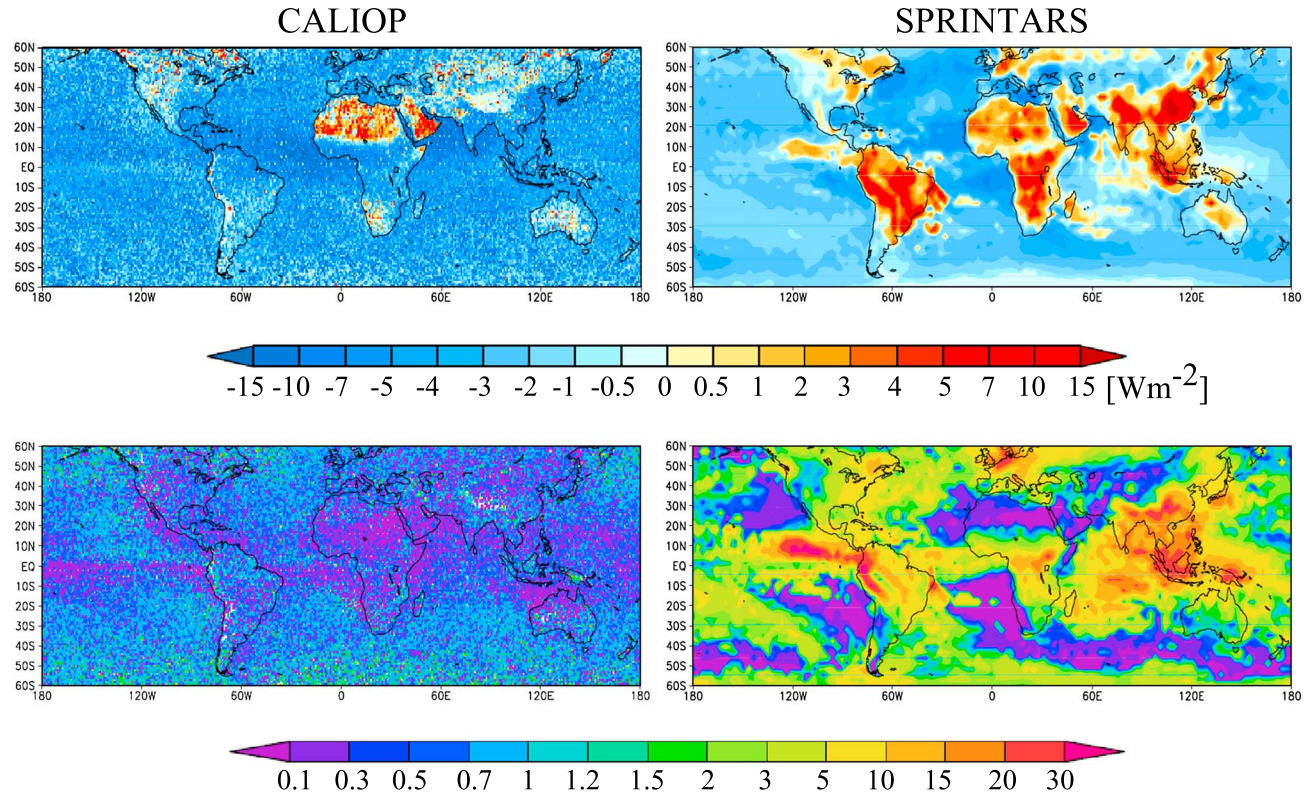

Figure 11. Same as Figure 10, but DARF (top) and COT (bottom) of the below-cloud case.

Table 2. Annual Mean AOT, SSA of Aerosols, COT, and Occurrence Probabilities Between 60°S and 60°N Under Clear-Sky, Cloudy-Sky, All-Sky Conditions for CALIOP and for SPRINTARS[a]

		Cloudy-Sky				
	Clear-Sky	Above-Cloud	Below-Cloud	Cloudy -Undetected	Total	All-Sky
CALIOP (+MODIS)						
AOT	0.109	0.192	0.362	0.000	0.066	0.074
SSA	0.89	0.87	0.90	-	0.88	0.89
COT	-	12.42	2.11	-	-	-
Occurrence probability	0.23	0.10	0.09	0.59	0.77	1.00
SPRINTARS						
AOT	0.111	-	-	-	0.158	0.133
SSA	0.91	-	-	-	0.91	0.91
COT	-	13.35	4.46	-	9.93	-
Occurrence probability	0.44	0.33	0.23	0.00	0.56	1.00

[a]The observation COT of above-cloud case is the sum of MODIS COT and CALIOP COT above MODIS cloud top height.

occurrence probability of clear-sky case is close to zero both in observation and model, while the cloudy-sky forcing of the model is more positive than the observation. Table 2 shows annual mean values of AOT, SSA of aerosols, COT, and occurrence probability from CALIOP and SPRINTARS. These parameters are important factors in determining DARF. At last, we summarize in Table 3 SW TOA DARFs averaged in the latitudinal area from 60°S to 60°N obtained in the preceding sections.

4.2. DARF at the Surface

[37] Figure 14 shows the annual mean distributions of the SW TOA DARF, surface DARF, and atmospheric absorption for all-sky condition. The annual zonal mean average of the TOA DARF, surface DARF, and atmospheric absorption for all-sky condition are -0.61, -4.63, and $+4.02$ Wm^{-2} and -0.58, -7.79, and $+7.21$ Wm^{-2} for CALIOP and SPRINTARS, respectively. Over China, India, and Africa, surface DARF is a large negative that is caused by the absorption of emitted aerosols. The surface DARF is much larger than the TOA DARF; thus, the patterns of atmospheric absorption of aerosols are quite similar to that of the surface DARF.

5. Discussions

5.1. Extrapolation of Aerosols Below Thick Clouds

[38] The uncertainty in the forcing evaluation is caused by a possible AOT underestimation by observation for the above-cloud case, because the CALIOP lidar detects aerosols only above optically thick clouds. Hence, we extrapolate the aerosol profile in this case toward levels below the cloud top height by assuming the maximum value of the aerosol extinction coefficient to the surface. We use the MODIS cloud top height for this extrapolation because the radiometer-sensed cloud top height is more radiatively effective for the radiation calculation. By this extrapolation, the zonal mean AOT from 60°S to 60°N in the above-cloud case increases from 0.192 to 0.444, and the annual mean DARF at TOA is more positive to +7.97, +0.45, and -0.32 Wm^{-2} under above-cloud, cloudy-sky, and all-sky cases, respectively. The main cause of this positive effect is enhanced light absorption by black carbon and dust particles within cloud layers. We need more validation studies of aerosol and cloud mixture by in situ measurements to finalize this point.

5.2. The Sensitivity Tests of CALIOP Optical Parameters

[39] The SSA is one of the important parameters to determine the forcing value. In this study, we used the CALIOP aerosol optical models (Table 1). A recent study reported SSA of biomass burning varied from 0.73 to 0.93 [*Johnson et al.*, 2008], and that of mineral dust is very weak [*Kaufman et al.*, 2001; *Dubovik et al.*, 2002; *Osborne et al.*, 2008; *Yoshida and Murakami*, 2008]. We, therefore, perform a sensitivity test that changes the imaginary index of refraction of aerosol particles from the standard CALIOP model value, m_i, [*Omar et al.*, 2009] to smaller values applying factors as $m_i * 0.5$ and $m_i * 0.0001$. Resulted DARFs under clear-sky, cloudy-sky, and all-sky conditions for CALIOP and SPRINTARS are listed in Table 3. The above-cloud DARF for $m_i * 0.5$ decreases to half of that for the standard case, and the cloudy-sky DARF changes to negative. Clear-sky and below-cloud DARFs increase about 30%. In the case of $m_i * 0.0001$, all aerosols are assumed as almost completely light scattering, so that the above-cloud DARF also alters its sign to negative. We should note that this sensitivity test is imperfect in a way that there is an inconsistency between reduced absorption models in the test and the CALIOP model used in the lidar data analysis.

5.3. Dependence of DARF on the Horizontal Resolutions

[40] The grid size of the observation ($1° \times 1°$) and the model ($2.8° \times 2.8°$) is different. Here we calculated the CALIOP-DARF at a horizontal resolution of $3° \times 3°$ for the examination of the dependence of the DARF on the horizontal resolution. Table 3 compares DARF values with different grid sizes of ($1° \times 1°$) and ($3° \times 3°$). The magnitude of DARF for the larger grid-box size is larger than that for the smaller grid-box size. The larger grid box sometimes includes the non-observation or non-aerosol detection smaller grid box. This causes the difference in computing the zonal average DARF, because the larger grid box covers the smaller number of smaller grid box. In our computation, the regional and global average of DARF of the larger grid-box size is larger than that of the smaller grid-box size. Aerosols

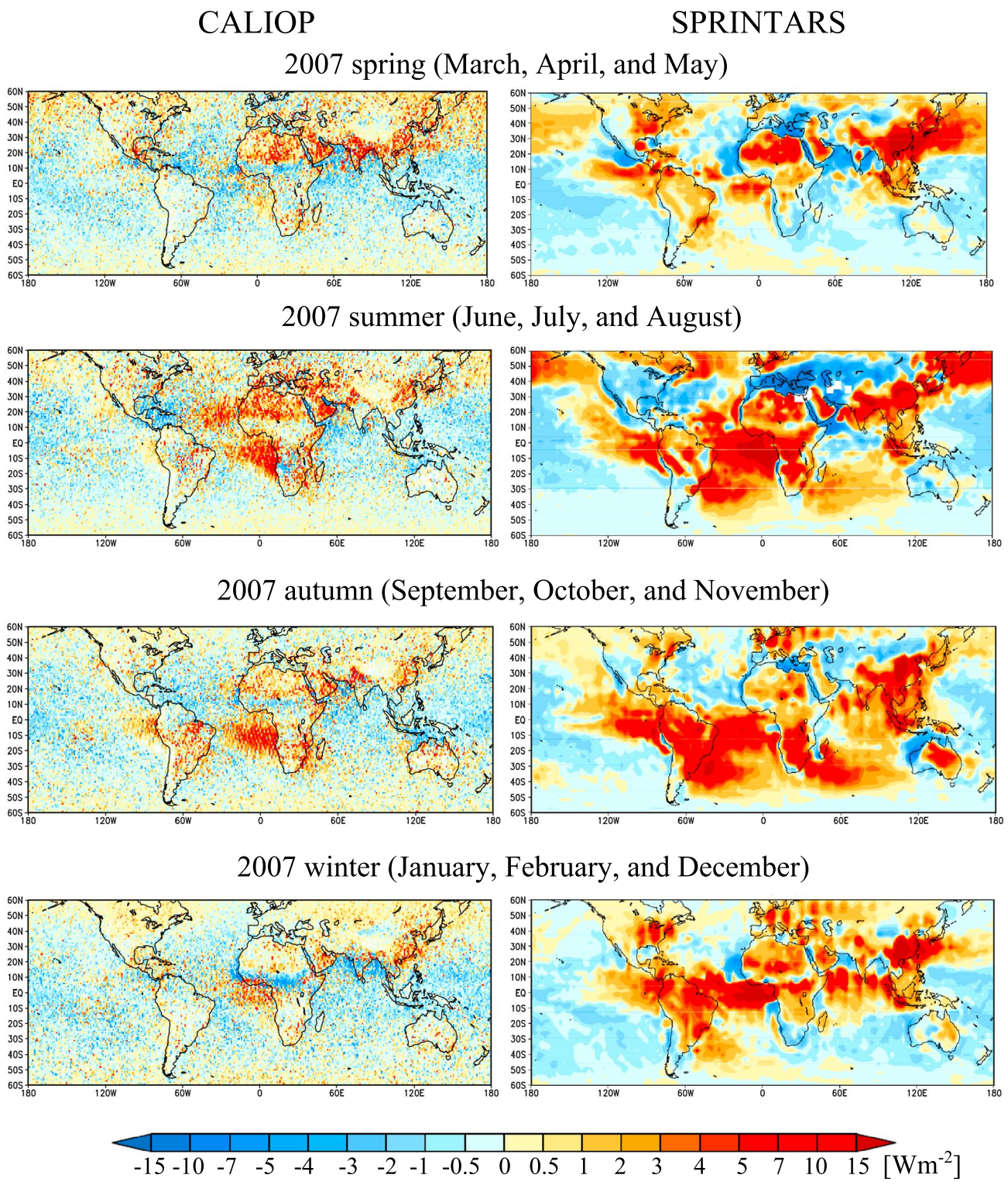

Figure 12. Same as Figure 8, but DARF under cloudy-sky case.

are rarely detected over the ocean around 60°S; however, once they are detected, the contribution for the regional and global average DARF computation becomes larger. The difference of the clear-sky forcing is smaller than that of cloudy-sky forcing, because the occurrence probability of the clear-sky case is larger than those of the above-cloud and below-cloud case (Figure 3). The difference of DARF between CALIOP and SPRINTARS becomes larger with the larger grid size of CALIOP. We think a degrading the satellite grid box to the coarse model box will lose the information that satellite data has. Therefore, we use the grid size (1° × 1°) for the observation in the main part of the present study.

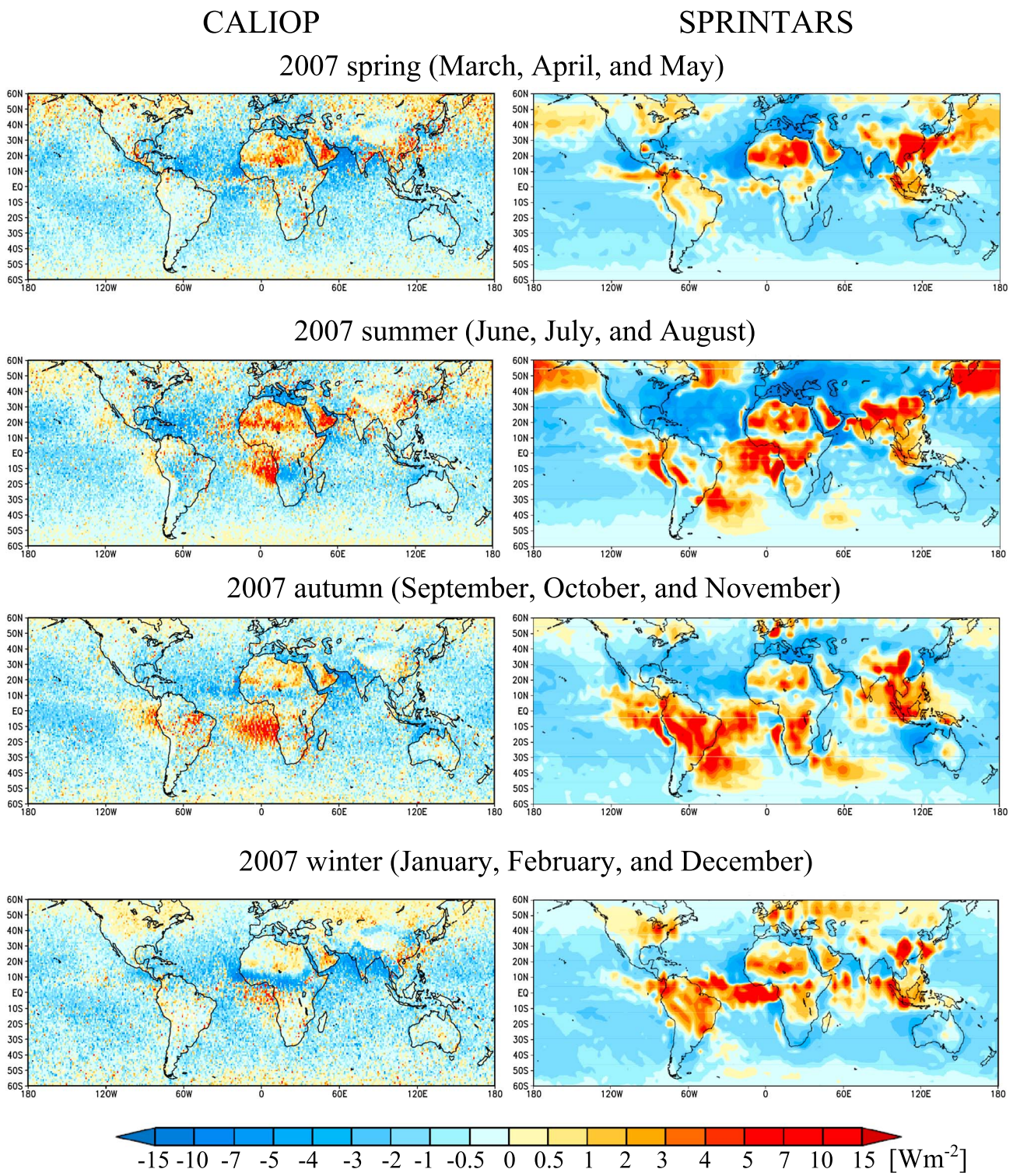

Figure 13. Same as Figure 8, but DARF under all-sky case.

5.4. Comparison of the Global Mean Clear-Sky DARF

[41] In this paper, DARF in the clear-sky case is defined as

$$DARF_{\text{clear-sky}} = P_a \times DARF_a, \tag{8}$$

where $DARF_a$ is the DARF calculated by using observed AOT and τ_a, and P_a is the occurrence probability of aerosols observed in the clear-sky condition (section A). In most of past studies, the conditional mean of aerosol existence, $DARF_a$, is used as the clear-sky DARF, and thus, we summarize the annual global mean values of $DARF_a$ in Table 4 for the comparison with previous studies. The global average of clear-sky DARF is -3.79 Wm^{-2} for CALIOP and -2.66 Wm^{-2} for SPRINTARS. *Kim and Ramanathan*

Table 3. Annual Mean SW DARF at TOA Between 60°S and 60°N Under Clear-Sky, Cloudy-Sky, All-Sky for CALIOP and SPRINTARS[a]

		Cloudy-Sky [Wm^{-2}]			
	Clear-Sky [Wm^{-2}]	Above-Cloud	Below-Cloud	Total	All-Sky [Wm^{-2}]
Zonal average (60°S–60°N)					
CALIOP	−2.97	+5.24	−5.52	+0.07	−0.61
SPRINTARS	−2.78	+2.51	−1.13	+1.07	−0.58
CALIOP $m_i * 0.5$	−3.74	+2.58	−7.42	−0.55	−1.27
CALIOP $m_i * 0.0001$	−5.14	−2.46	−10.87	−1.72	−2.47
CALIOP (3° × 3°)	−3.17	+6.15	−8.63	−0.12	−0.81
Land					
CALIOP	−2.29	+8.08	−2.98	+0.73	−0.12
SPRINTARS	−1.63	+2.89	+1.44	+2.18	+0.12
CALIOP $m_i * 0.5$	−3.70	+4.32	−6.33	−0.25	−1.20
CALIOP $m_i * 0.0001$	−6.19	−2.82	−12.32	−2.06	−3.12
CALIOP (3° × 3°)	−2.50	+9.02	−5.11	+0.59	−0.28
Ocean					
CALIOP	−3.21	+4.21	−6.43	−0.16	−0.79
SPRINTARS	−3.19	+2.38	−2.04	+0.68	−0.83
CALIOP $m_i * 0.5$	−3.76	+1.95	−7.82	−0.66	−1.29
CALIOP $m_i * 0.0001$	−4.76	−2.33	−10.34	−1.60	−2.23
CALIOP (3° × 3°)	−3.41	+5.11	−9.90	−0.38	−1.00

[a]The radiative forcing of CALIOP is shown for the refractive indices of aerosol particles, m_i, $m_i * 0.5$, and $m_i * 0.0001$ (see text for definition).

[2008] compared TOA shortwave DARF under clear-sky. DARF using ground-based and satellite-based observation data is −5.9 Wm^{-2} and that of AeroCom is −3.3 Wm^{-2}. The observation value in this study is between model average and measurement-base average, and the simulation value in this study is smaller than these. *Yu et al*. [2006] compared the clear-sky DARF from satellite retrievals and model simulations. The average of satellite-derived and model values over the land and ocean is listed in Table 4 for comparison. They reported that SPRINTARS shows the smallest clear-sky forcing among the satellite-derived values and models results. *Goto et al*. [2011] pointed out that the magnitude of shortwave plus longwave DARF of SPRINTARS is smaller in remote area and larger near source regions due to weak transportation of aerosols to upper altitudes. BC and dust are not transported to the remote areas in SPRINTARS [*Koch et al*., 2009; *Huneeus et al*., 2011]. These are consistent with the results in this study and indicate that the absorption of aerosols over the land is large in SPRINTARS and the TOA SW DARF under clear-sky is −1.53 Wm^{-2}. This value is less than half of CALIOP and *Yu et al*. [2006]. The CALIOP TOA DARF is smaller, and surface DARF is larger than those of *Yu et al*. [2006]. The CALIOP DARFs for $m_i * 0.5$ are close to that of *Yu et al*. [2006]. These indicate that aerosol models of CALIOP and SPRINTARS are absorbing models stronger than those in the past studies. In the case of $m_i * 0.0001$, all aerosols almost completely scatter the sunlight, so that the TOA DARF becomes close to the surface DARF and atmospheric absorption of aerosols is +0.21 Wm^{-2}.

[42] The zonal average between 60°S and 60°N of SPRINTARS clear-sky DARF is about 5% more than the global average value, because AOT is quite small in high-latitude regions and the zonal average AOT is larger than the global average. In CALIOP, the zonal average DARF listed in Table 3 is smaller than the global average in Table 4, because the occurrence probability P_a is 0.67 between 60°S and 60°N and this has a larger effect than the difference of AOT between the zone and the globe in this study. This indicates that taking into account of optically thin aerosols that is undetected by sensors or not causes the different regional and global average values and becomes one of the reasons that the measurement-retrieved DARF is larger than the model values.

6. Conclusions

[43] We estimated the shortwave DARF at TOA and surface under clear-sky, cloudy-sky, and all-sky conditions using the observation data from space-borne CALIOP lidar and MODIS sensor and the simulation results from SPRINTARS. We calculated DARF in four scenarios: the clear-sky case, the above-cloud case, the below-cloud case, and the cloudy-undetected case. The cloudy-sky DARF was estimated by the DARF in the latter three scenarios and the occurrence probability of each scenario, and the all-sky DARF is the combination of clear-sky and cloudy-sky DARF with weights of the cloud occurrence at the limited zone from 60°S to 60°N. The COT derived from Aqua MODIS was applied for the CALIOP cloud profile in the above-cloud case; aerosol and cloud fields from 60°S to 60°N were obtained from CALIOP and MODIS sensors throughout the year of 2007. Therefore, we analyzed AOT, COT, SSA, and the occurrence probabilities in this zonal region.

[44] At the TOA, annual zonal averages of the shortwave DARFs under clear-sky, cloudy-sky, and all-sky conditions were −2.97, +0.07, and −0.61 Wm^{-2} for CALIOP, respectively, and −2.78, +1.07, and −0.58 Wm^{-2} for SPRINTARS, respectively. At the surface, SW DARFs under clear-sky, cloudy-sky, and all-sky conditions were −8.90, −3.46, and −4.63 Wm^{-2} for CALIOP, respectively, and −9.11, +7.31, and −7.79 Wm^{-2} for SPRINTARS, respectively. The zonal average clear-sky forcing was about 5% higher than the global average value, because aerosol amount over high-latitude regions is quite small. Under clear-sky condition, the TOA forcing of CALIOP and SPRINTARS are smaller and the atmospheric absorption of aerosols are larger than previous studies. This indicates

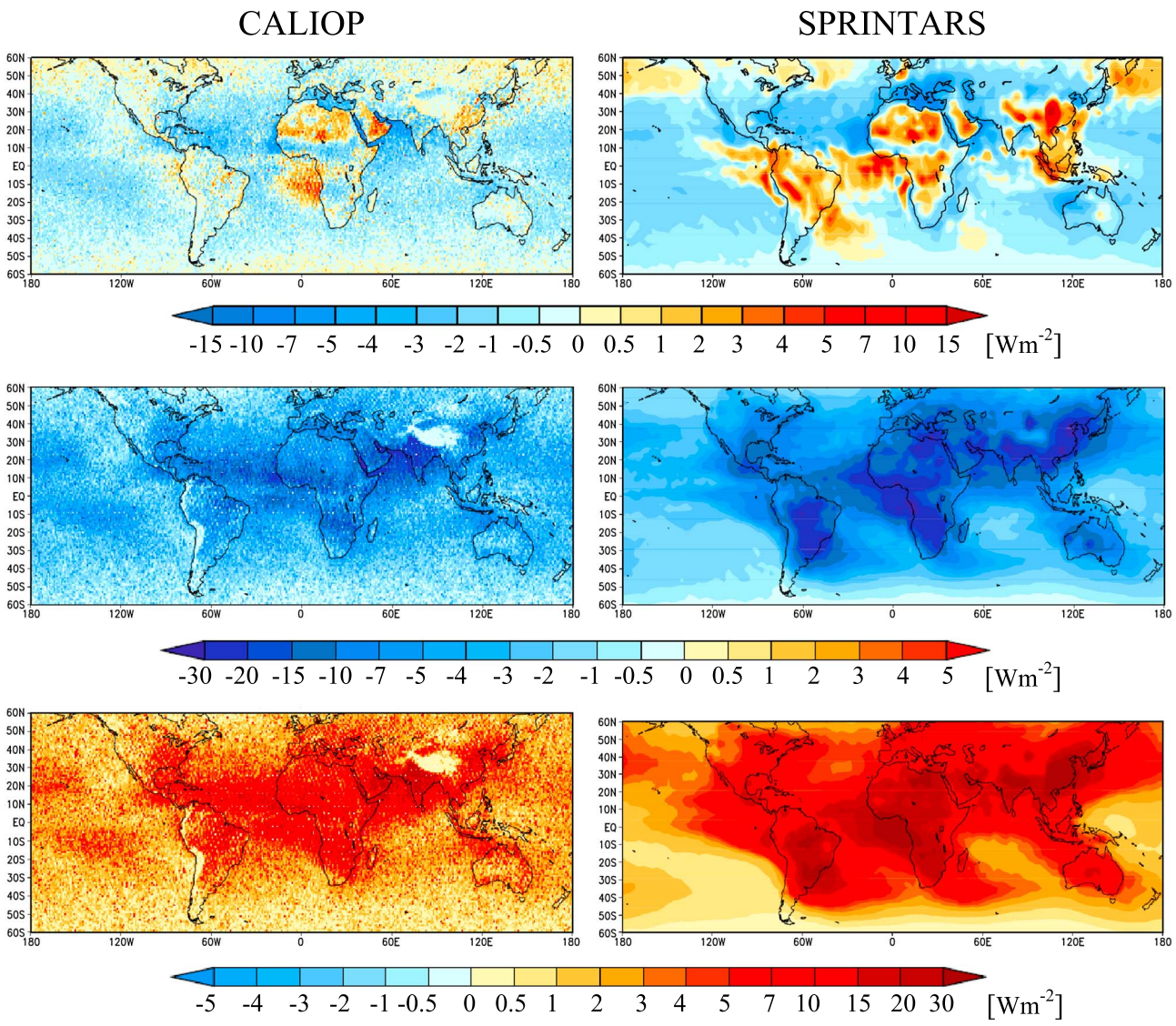

Figure 14. Annual mean distributions of the shortwave TOA DARF (top), surface DARF (middle), and atmospheric absorption (bottom) for all-sky condition from the CALIOP observation (left) and simulated results by SPRINTARS (right).

that aerosol models of CALIOP and SPRINTARS are strong absorbing models. The improvement of the optical parameters of aerosol models of CALIOP and SPRINTARS and more detailed and longer-term analysis are required to estimate more precise value of the regional DARF.

[45] The results showed that the TOA forcing over desert regions caused by dust with SSA of 0.92 is positive regardless of cloud existence, due to high ground albedo. Off southern Africa, smoke aerosols with SSA of 0.84 above low-level clouds are observed and simulated and the annual mean TOA cloudy-sky DARF is more than +3 Wm^{-2}, consistent with past studies. Aerosols with SSA of 0.96 within optically thin clouds cause TOA negative forcing, while those within optically thick clouds cause TOA positive forcing. This is because the scattering of aerosols is larger than the absorption of aerosols within optically thin

Table 4. Annual Global Mean DARF at TOA and Surface Under Clear-Sky for CALIOP and SPRINTARS[a]

	DARF (TOA) [Wm^{-2}]			DARF (Surface) [Wm^{-2}]		
	Global	Land	Ocean	Global	Land	Ocean
CALIOP	−3.79	−2.69	−4.24	−11.43	−14.04	−10.38
CALIOP (m_i * 0.5)	−4.81	−4.46	−4.95	−9.72	−11.70	−8.92
CALIOP (m_i * 0.0001)	−6.66	−7.62	−6.28	−6.87	−7.75	−6.51
SPRINTARS	−2.66	−1.53	−3.10	−8.64	−11.81	−7.43
Yu et al. [2006]	-	-4.9 ± 0.7	-5.5 ± 0.2	-	-11.8 ± 1.9	-8.8 ± 0.7

[a]The radiative forcing of CALIOP is shown for the refractive indices of aerosol particles, m_i, m_i * 0.5, and m_i * 0.0001 (see text for definition). The DARF in *Yu et al.* [2006] are listed for comparison.

clouds and the small absorption of aerosols is enhanced and scattering of aerosols becomes smaller within optically thick clouds. This indicates that aerosols within optically thick clouds cause positive forcing in our radiative transfer calculation, regardless of SSA.

[46] CALIOP has only one daytime observation at fixed local time for a target location, so that we have no other choice than using the same observed vertical stratification of aerosol and cloud in the DARF calculation of every hour, which will cause an error in the evaluated DARF. However, we should reiterate that our main emphasis is evaluation of the effect of aerosol and cloud stratifications such as clear-sky, above-cloudy, below-cloud, and cloudy-undetected cases. In conclusion, we would like to stress that errors that come from these assumptions might not be too large to change our findings. On the other hand, it is important that the vertical distributions of aerosols and clouds of various models are compared to those of CALIOP and CloudSat at the same local time.

[47] We also need to discuss the sampling method in the process of construction of the aerosol and cloud laden atmosphere in the present study. We used the monthly mean profiles of aerosols and clouds in three cases (clear-sky, above-cloud, and below-cloud). Each CALIOP observation retrieves only one type of the particle (aerosol or cloud) at the resolution grid and cannot measure how aerosol and cloud particles coexist in optically thick cloud layers. In this situation, there is a benefit of using the monthly profiles in above-cloud and below-cloud cases from CALIOP because we can get simultaneous aerosol and cloud profiles at the same altitude. This information of aerosol and cloud stratification can be used to study heights of aerosol and cloud layers at all locations of the globe. However, it brings an ambiguity regarding how aerosol and cloud particles are mixed in the cloud layer. Additionally, CALIOP aerosol products are of a 5 km horizontal resolution averaging 15 lidar shots, and it is possible that the forcing for the horizontally averaged atmosphere is different from the mean of forcings obtained by each lidar shot. In this case, however, there is a difficulty of using each lidar shot data because aerosols are not dense enough to be retrieved from every shot [*Vaughan et al.*, 2009]. The monthly mean parameters will cause an error in the evaluation of DARF. On the other hand, CALIOP lidar sensitivity is not so high that the shot by shot data includes a large ambiguity in the retrieved aerosol and cloud parameters. There needs to be a thorough investigation in the future to identify the optimal sampling average for the DARF estimation, and we would like to leave these difficult questions for future works, especially to simultaneous use of satellite observation and high resolution aerosol and cloud modeling.

Appendix A

[48] We have four scenarios for radiative transfer calculation, i.e., clear-sky, above-cloud, below-cloud, and cloudy-undetected cases. The conditional occurrence probability of aerosols observed in the clear-sky condition is given as

$$P_a = \frac{N_a}{N_{\text{clear-sky}}}, \tag{A1}$$

where N_a is the pixel count where aerosols are observed in the clear-sky condition and $N_{\text{clear-sky}}$ is the pixel count in the clear-sky condition. We use the conditional AOT for radiative transfer calculations defined as

$$\tau_a = \frac{\tau_{a,\text{sum}}}{N_a}, \tag{A2}$$

at wavelength of 532 nm where $\tau_{a,\text{sum}}$ is the sum of AOT observed at clear-sky pixels. Clear-sky AOT shown in Figure 5 is given as

$$\tau_{\text{clear-sky}} = \frac{\tau_{a,\text{sum}}}{N_{\text{clear-sky}}} = P_a \frac{\tau_{a,\text{sum}}}{N_a} \tag{A3}$$

Shortwave direct aerosol forging in the clear-sky case is defined as

$$DARF_{\text{clear-sky}} = P_a \times DARF_a, \tag{A4}$$

where $DARF_a$ is the DARF calculated by using τ_a.

[49] In a similar way, P_{ac} is the conditional occurrence probability of the above-cloud case, P_{bc} is that of the below-cloud case, and P_{uc} is that of the cloudy-undetected case:

$$P_{ac} = \frac{N_{ac}}{N_{\text{cloudy-sky}}}, \quad P_{bc} = \frac{N_{bc}}{N_{\text{cloudy-sky}}}, \quad \text{and} \tag{A5}$$

$$P_{uc} = \frac{N_{\text{cloudy-sky}} - N_{ac} - N_{bc}}{N_{\text{cloudy-sky}}},$$

$$P_{ac} + P_{bc} + P_{uc} = 1, \tag{A6}$$

where N_{ac}, N_{bc}, and $N_{\text{cloudy-sky}}$ are the pixel counts of above-cloud, below-cloud, and cloudy-sky cases, respectively. P_{uc} is equal to zero for SPRINTARS. τ_{ac} and τ_{bc} are AOTs for radiation calculations for above-cloud and below-cloud cases, respectively,

$$\tau_{ac} = \frac{\tau_{ac,\text{sum}}}{N_{\text{ac}}} \quad \text{and} \quad \tau_{bc} = \frac{\tau_{bc,\text{sum}}}{N_{\text{bc}}} \tag{A7}$$

where $\tau_{ac,\text{sum}}$ and $\tau_{bc,\text{sum}}$ are sums of AOT observed in above-cloud and below-cloud cases, respectively. AOT in the cloudy-sky case is given as

$$\tau_{\text{cloudy-sky}} = \frac{\sum_{i=ac,bc,uc} \tau_{i,\text{sum}}}{N_{\text{cloudy-sky}}} = \sum_{i=ac,bc} P_i \cdot \tau_i + 0 = \sum_{i=ac,bc} P_i \cdot \tau_i. \tag{A8}$$

The DARF in the cloudy-sky condition is then given as

$$DARF_{\text{cloudy-sky}} = \sum_{i=ac,bc,uc} P_i \times DARF_i \approx \sum_{i=ac,bc} P_i \times DARF_i + 0 = \sum_{i=ac,bc} P_i \times DARF_i. \tag{A9}$$

where we assume that DARF of the cloudy-undetected case is close to zero, because optically thick clouds dominantly scatter the incident sunlight.

[50] The DARF under all-sky condition is given as

$$DARF_{\text{all-sky}} = P_{\text{clear-sky}} \times DARF_{\text{clear-sky}} \quad \text{(A10)}$$

$$+P_{\text{cloudy-sky}} \times DARF_{\text{cloudy-sky}}.$$

[51] We use similar formulae for radiative transfer calculations with model SPRINTARS-simulated values. In the model, we assume $P_a = 1$ and $P_{ac} + P_{bc} = 1$, because all the aerosols, including a part not observed by CALIOP, are simulated by the model. The same cloudy-sky AOT is used for radiation calculations for above-cloud and below-cloud cases: $\tau_{\text{clear-sky}} = \tau_a$ and $\tau_{\text{cloudy-sky}} = \tau_{ac} = \tau_{bc}$. AOT at 532 nm is used for CALIOP and that of 550 nm is used for SPRINTARS.

[52] **Acknowledgments.** Part of this research was supported by funds from MOE/GOSAT, MOE/GER fund A1101, JST/CREST/EMS/TEEDDA, JAXA/EarthCARE and GCOM-C, MEXT/VL for climate diagnostics, MEXT/RECCA/SALSA, MEXT/KAKENHI/Innovative Areas 2409. We would like to thank D. Goto for providing the SPRINTARS simulation results and T. Nishizawa for discussing the SSA calculation and valuable comments.

References

d'Almeida, G. A., P. Koepke, and E. P. Shettle (1991), *Atmospheric Aerosols: Global Climatology and Radiative Characteristics*, A. Deepak Publishing, Hampton, VA.

Chand, D., T. L. Anderson, R. Wood, R. J. Charlson, Y. Hu, Z. Liu, and M. Vaughan (2008), Quantifying above-cloud aerosol using spaceborne lidar for improved understanding of cloudy-sky direct climate forcing, *J. Geophys. Res.*, *113*, D13206, doi:10.1029/2007JD009433.

Chand, D., R. Wood, T. L. Anderson, S. K. Satheesh, and R. J. Charlson (2009), Satellite-derived direct radiative effect of aerosols dependent on cloud cover, *Nat. Geosci.*, *2*, 181–184, doi:10.1038/NGE0437.

Coddington, O. M., P. Pilewskie, J. Redemann, S. Platnick, P. B. Russell, K. S. Schmidt, W. J. Gore, J. Livingston, G. Wind, and T. Vukicevic (2010), Examining the impact of overlying aerosols on the retrieval of cloud optical properties from passive remote sensing, *J. Geophys. Res.*, *115*, D10211, doi:10.1029/2009JD012829.

De Graaf, M., L. G. Tilstra, P. Wang, and P. Stammes (2012), Retrieval of the aerosol direct radiative effect over clouds from spaceborne spectrometry, *J. Geophys. Res.*, *117*, D07207, doi:10.1029/2011JD017160.

Deepak, A., and H. G. Gerber (Eds.) (1983), Report of the experts meeting on aerosols and their climatic effects, World Meteorological Organization, Geneva, Switzerland, *Rep. WCP-55*, 107 pp.

Dubovik, O., B. Holben, T. F. Eck, A. Smirnov, Y. J. Kaufman, M. D. King, D. Tanré, and I. Slutsker (2002), Variability of absorption and optical properties of key aerosol types observed in worldwide locations, *J. Atmos. Sci.*, *59*, 590–608.

Fraser, R. S., and Y. J. Kaufman (1985), The relative importance of aerosol scattering and absorption in remote sensing, *IEEE Trans. Geosci. Remote Sens. GE-23*, 625–633.

Gao, W., Q. F. Lu, Z. Q. Gao, W. L. Wu, B. Y. Du, and J. Slusser (2006), Analysis of temporal variations of albedo from MODIS, in *Remote Sensing and Modeling of Ecosystems for Sustainability III*, pp. 62981G-1–62981G-7, SPIE, Bellingham, WA, USA.

Goto, D., T. Nakajima, T. Takemura, and K. Sudo (2011), A study of uncertainties in the sulfate distribution and its radiative forcing associated with sulfur chemistry in a global aerosol model, *Atmos. Chem. Phys.*, *11*, 10,889–10,910, doi:10.5194/acp-11-10889-2011.

Haywood, J. M., and K. P. Shine (1997), Multi-spectral calculations of the radiative forcing of tropospheric sulphate and soot aerosols using a column model, *Quart. J. R. Meteor. Soc.*, *123*, 1907–1930.

Haywood, J. M., S. R. Osborne, and S. J. Abel (2004), The effect of overlying absorbing aerosol layers on remote sensing retrievals of cloud effective radius and cloud optical depth. *Q. J. R. Meteorol. Soc.*, *130*, 779–800.

Hobbs, P. V., J. S. Reid, R. A. Kotchenruther, R. J. Ferek, and R. Weiss (1997), Direct radiative forcing by smoke from biomass burning, *Science*, *275*, 1776–1778.

Hu, Y., M. Vaughan, Z. Liu, K. Powell, and S. Rodier (2007), Retrieving optical depths and lidar ratios for transparent layers above opaque water clouds from CALIPSO lidar measurements, *IEEE Trans. Geosci. Remote Sens. Lett.*, *4*, 523–526.

Huneeus, N., et al. (2011), Global dust model intercomparison in AeroCom phase I, *Atmos. Chem. Phys.*, *11*, 7781–7816, doi:10.5194/acp-11-7781-2011.

Intergovernmental Panel on Climate Change (IPCC) (2007), *Climate Change 2007; The Physical Science Basis*, edited by S. Solomon, D. Qin, M. Manning, M. Marquis, K. Aveyt, M. M. B. Tignor, H. L. Miller Jr., and Z. Chen, 996 pp., Cambridge University Press, Cambridge, United Kingdom and New York, NY, USA.

Johnson, B. T., S. R. Osborne, J. M. Haywood, and M. A. J. Harrison (2008), Aircraft measurements of biomass burning aerosols over West Africa during DABEX, *J. Geophys. Res.*, *113*, D00C06, doi:10.1029/2007JD009451.

K-1 Model Developers (2004), in *K-1 coupled GCM (MIROC) description*, edited by H. Hasumi and S. Emori, K-1 Tech. Rep. 1, 34 pp., Center for Climate System Research, University of Tokyo, Tokyo, Japan.

Kalnay, E., et al. (1996), The NCEP/NCAR 40-year reanalysis project, *Bull. Am. Meteorol. Soc.*, *77*, 437–471.

Kaufman, Y. J., D. Tanre, O. Dubovik, A. Karnieli, and L. A. Remer (2001) Absorption of sunlight by dust as inferred from satellite and ground-based remote sensing, *Geophys. Res. Lett.*, *28*, 1479–1482.

Keil, A., and J. M. Haywood (2003), Solar radiative forcing by biomass burning aerosol particles during SAFARI 2000: A case study based on measured aerosol and cloud properties, *J. Geophys. Res.*, *108*, 8467, doi:10.1029/2002JD002315.

Kim, D., and V. Ramanathan (2008), Solar radiation budget and radiative forcing due to aerosols and clouds, *J. Geophys. Res.*, *113*, D02203, doi:10.1029/2007JD008434.

Kittaka, C., D. M. Winker, M. A. Vaughan, A. Omar, and L. A. Remer (2011), Intercomparison of column aerosol optical depths from CALIPSO and MODIS-Aqua, *Atmos. Meas. Technol.*, *4*, 131–141, doi:10.5194/amt-4-131-2011.

Kneizys P. X., E. P. Shettle, L. W. Abreu, J. H. Chetwynd, G. P. Anderson, W. O. Gallery, J. E. A. Selby, and S. A. Clough (1988), Users Guide to LOWTRAN 7, *Rep. AFGL-TR-88-0177*, *Bedford*, *MA*: *Air Force Geophys. Lab.*

Koch, D., et al. (2009), Evaluation of black carbon estimations in global aerosol models, *Atmos. Chem. Phys.*, *9*, 9001–9026, doi:10.5194/acp-9-9001-2009.

Lin, J.-L., et al. (2006), Tropical intraseasonal variability in 14 IPCC AR4 climate models. Part I: Convective signals, *J. Clim.*, *19*, 2665–2690.

Liu, Z., M. A. Vaughan, D. M. Winker, C. Kittaka, B. J. Getzewich, R. E. Kuehn, A. Omar, K. Powell, C. R. Trepte, and C. A. Hostetler (2009), The CALIPSO lidar cloud and aerosol discrimination: Version 2 algorithm and initial assessment of performance, *J. Atmos. Oceanic Technol.*, *26*, 1198–1213.

Martins, J. V., P. Artaxo, P. V. Hobbs, C. Liousse, H. Cachier, Y. Kaufman, and A. Plana-Fattori (1996), Particle size distributions, elemental compositions, carbon measurements, and optical properties of smoke from biomass burning in the Pacific Northwest of the United States, in *Biomass Burning and Global Change*, vol. *2*, edited by J. S. Levine, pp. 716–732, MIT Press, Cambridge, Mass.

Nakajima, T., and M. Tanaka (1983), Effect of wind-generated waves on the transfer of solar radiation in the atmosphere-ocean system, *J. Quant. Spectrosc. Radiat. Transfer*, *29*, 521–537.

Nakajima, T., and M. Tanaka (1986), Matrix formulations for the transfer of solar radiation in a plane-parallel scattering atmosphere, *J. Quant. Spectrosc. Radiat. Transfer*, *35*, 13–21.

Nakajima, T., and M. Tanaka (1988), Algorithms for radiative intensity calculations in moderately thick atmospheres using a truncation approximation. *J. Quant. Spectrosc. Radiat. Transfer*, *40*, 51–69.

Nakajima, T., et al. (2007), Overview of the Atmospheric Brown Cloud East Asian Regional Experiment 2005 and a study of the aerosol direct radiative forcing in East Asia, *J. Geophys. Res.*, *112*, D24S91, doi:10.1029/2007JD009009.

Omar, A. H., et al. (2009), The CALIPSO automated aerosol classification and lidar ratio selection algorithm, *J. Atmos. Oceanic Technol.*, *26*, 1994–2014.

Osborne, S. R., B. T. Johnson, J. M. Haywood, A. Baran, M. Harrison, and C. L. McConnell (2008), Physical and optical properties of mineral dust aerosol during the dust and biomass-burning experiment, *J. Geophys. Res.*, *113*, D00C03, doi:10.1029/2007JD009551.

Roesch, A., C. Schaaf, and F. Gao (2004), Use of Moderate-Resolution Imaging Spectroradiometer bidirectional reflectance distribution function products to enhance simulated surface albedos, *J. Geophys. Res.*, *109*, D12105, doi:10.1029/2004JD004552.

Ruggaber, A., R. Dlugi, and T. Nakajima (1994), Modelling of radiation quantities and photolysis frequencies in the troposphere, *J. Atmos. Chem.*, *18*, 171–210.

Schaaf, C. B., et al. (2002), First operational BRDF, albedo nadir reflectance products from MODIS, *Remote Sens. Environ.*, *83*, 135–148.

Schulz, M., et al. (2006), Radiative forcing by aerosols as derived from the AeroCom present-day and pre-industrial simulations, *Atmos. Chem. Phys.*, *6*, 5225–5246.

Sutherland, R. A., and R. K. Khanna (1991), Optical properties of organic-based aerosols produced by burning vegetation, *Aerosol Sci. Technol.*, *14*, 331–342.

Takemura, T., H. Okamoto, Y. Maruyama, A. Numaguti, A. Higurashi, and T. Nakajima (2000), Global three-dimensional simulation of aerosol optical thickness distribution of various origins, *J. Geophys. Res.*, *105*, 17,853– 17,873.

Takemura, T., T. Nakajima, O. Dubovik, B. N. Holben, and S. Kinne (2002), Single scattering albedo and radiative forcing of various aerosolspecies with a global three-dimensional model, *J. Clim.*, *15*, 333–352.

Takemura, T., T. Nozawa, S. Emori, T. Y. Nakajima, and T. Nakajima (2005), Simulation of climate response to aerosol direct and indirect effects with aerosol transport-radiation model, *J. Geophys. Res.*, *110*, D02202, doi:10.1029/2004JD005029.

Tang, I. N., and H. R. Munkelwitz (1994), Water activities, densities, and refractive indices of aqueous sulfates and sodium nitrate droplets of atmospheric importance, *J. Geophys. Res.*, *99*, 18,801–18,808.

Vaughan, M., K. Powell, R. Kuehn, S. Young, D. Winker, C. Hostetler, W. Hunt, Z. Liu, M. McGill, and B. Getzewich (2009), Fully automated detection of cloud and aerosol layers in the CALIPSO lidar measurements, *J. Atmos. Oceanic Technol.*, *26*, 2034–2050.

Winker, D. M., M. Vaughan, A. Omar, Y. Hu, K. Powell, Z. Liu, W. Hunt, and S. A. Young (2009), Overview of the CALIPSO mission and CALIOP data processing algorithms, *J. Atmos. Oceanic Technol.*, *26*, 2310–2323.

Winker, D. M., et al. (2010), The CALIPSO Mission: A global 3D view of aerosols and clouds, *Bull. Amer. Meteor. Soc.*, *91*, 1211–1229.

Yoshida, M., and H. Murakami (2008), Dust absorption averaged over the Sahara inferred from moderate resolution imaging spectroradiometer, *Appl. Opt.*, *47*, 1995–2003.

Young, S. A., and M. A. Vaughan (2009), The retrieval of profiles of particulate extinction from Cloud Aerosol Lidar Infrared Pathfinder Satellite Observations (CALIPSO) data: Algorithm description, *J. Atmos. Oceanic Technol.*, *26*, 1105–1119, doi:10.1175/2008 JTECHA1221.1.

Yu, H., R. E. Dickinson, M. Chin, Y. J. Kaufman, M. Zhou, L. Zhou, Y. Tian, O. Dubovik, and B. N. Holben (2004), Direct radiative effect of aerosols as determined from a combination of MODIS retrievals and GOCART simulations, *J. Geophys. Res.*, *109*, D03206, doi:10.1029/2003JD003914.

Yu, H., et al. (2006), A review of measurement-based assessments of the aerosol direct radiative effect and forcing, *Atmos. Chem. Phys.*, *6*, 613–666, doi:10.5194/acp-6-613-2006.